AWARD NUMBER: W81XWH-17-1-0526

TITLE: Iron Chelation Enhances TAM and Triple-Negative Breast Cancer Cell Death

PRINCIPAL INVESTIGATOR: Ronald Blasberg

CONTRACTING ORGANIZATION: Sloan Kettering Institute for Cancer Research
New York, NY 10065

REPORT DATE: October 2018

TYPE OF REPORT: Annual

PREPARED FOR: U.S. Army Medical Research and Materiel Command
Fort Detrick, Maryland 21702-5012

DISTRIBUTION STATEMENT: Approved for Public Release;
Distribution Unlimited

REPORT DOCUMENTATION PAGE

Form Approved
OMB No. 0704-0188

1. REPORT DATE	2. REPORT TYPE	3. DATES COVERED
October 2018	Annual	15 Sep 2017 – 14 Sep 2018

4. TITLE AND SUBTITLE

Iron Chelation Enhances TAM and Triple-Negative Breast Cancer Cell Death

5a. CONTRACT NUMBER

5b. GRANT NUMBER
W81XWH-17-1-0526

5c. PROGRAM ELEMENT NUMBER

6. AUTHOR(S)
Jason Koutcher (initiating PI) and Ronald Blasberg (Partnering PI)

E-Mail: koutchej@mskcc.org ; blasberr@mskcc.org

5d. PROJECT NUMBER

5e. TASK NUMBER

5f. WORK UNIT NUMBER

7. PERFORMING ORGANIZATION NAME(S) AND ADDRESS(ES)

Sloan Kettering Institute for
Cancer Research
1275 York Avenue, New York NY
10065-6007

8. PERFORMING ORGANIZATION REPORT NUMBER

9. SPONSORING / MONITORING AGENCY NAME(S) AND ADDRESS(ES)

U.S. Army Medical Research and Materiel Command
Fort Detrick, Maryland 21702-5012

10. SPONSOR/MONITOR'S ACRONYM(S)

11. SPONSOR/MONITOR'S REPORT NUMBER(S)

12. DISTRIBUTION / AVAILABILITY STATEMENT

Approved for Public Release; Distribution Unlimited

13. SUPPLEMENTARY NOTES

14. ABSTRACT The goal of this study is to complete preclinical testing of Deferiprone (DFP), an iron chelator in clinical use for non-oncologic diseases. We will demonstrate the sensitivity of triple negative breast cancer (TNBC) to DFP as a single agent, and in combination with immune modulation therapy and chemotherapy. We will determine if imaging of changes in iron or metabolism, using MRI is a biomarker of DFP efficacy. Studies of in vitro effects of DFP, followed by in vivo effects, followed by the effects of adding other drugs (checkpoint inhibitors and paclitaxel)were proposed, in addition to studies of the effects of these drugs on cell cycle and immune activity/function. We have demonstrated that DFP has an IC50 (therapeutic concentration) within the range achieved after clinical doses in many cancer cell lines, enhances paclitaxel in multiple cell lines, and that there is less iron in the 4T1 TNBC line than other cell lines

15. SUBJECT TERMS
Breast cancer, iron imaging, MRI, metabolism

16. SECURITY CLASSIFICATION OF:			17. LIMITATION OF ABSTRACT	18. NUMBER OF PAGES	19a. NAME OF RESPONSIBLE PERSON
a. REPORT	b. ABSTRACT	c. THIS PAGE			USAMRMC
Unclassified	Unclassified	Unclassified	Unclassified	10	19b. TELEPHONE NUMBER *(include area code)*

Table of Contents

Page

Introduction

The goal of this study is to complete preclinical testing of Deferiprone (DFP), an iron chelator in clinical use for non-oncologic diseases. We propose to demonstrate the sensitivity of TNBC to DFP as a single agent, and in combination with immune modulation therapy (checkpoint inhibitors) and chemotherapy (paclitaxel). We will determine if imaging of changes in iron content using magnetic resonance imaging can serve as a biomarker of DFP efficacy. Studies were planned to be performed sequentially by first studying in vitro effects of DFP, followed by in vivo effects, followed by the effects of adding other drugs (checkpoint inhibitors and paclitaxel). Effects of these drugs on cell cycle and immune effects were also proposed

Keywords:

Breast cancer, MRI, iron, chelators, Deferiprone, macrophages, metabolism, checkpoint inhibitors

Major Goals of Projects:

Aim 1 Determine how inhibition of iron metabolism and OXPHOS impedes TAM function and metabolism, and reduces proliferation of TAMs and TNBC cells.
Aim 2: *Develop and validate non-invasive MRI methods to quantitatively and spatially monitor tumor and tissue iron and TAM infiltration, to detect changes induced by macrophage focused therapy.*
Aim 3: *Determine if inhibition of iron metabolism, TCA cycle, and OXPHOS by DFP: i) inhibits tumor growth, and ii) enhances responses to chemotherapy and immune checkpoint inhibitors in orthotopic TNBC*

Accomplishments:

1. Methodology for iron imaging in breast cancer has been developed and reported (Refs 4,5)
2. This methodology was applied to the 4T1 breast cancer model as proposed (see Figs 2-5).
3. A significant amount of data has been accumulated studying the effect of DFP on immune modulation but awaits analysis
4. The experimental setup for studying tumor cell metabolism has been completed and shown to work – this had a series of setbacks as discussed below but is now ready.

What was Accomplished:

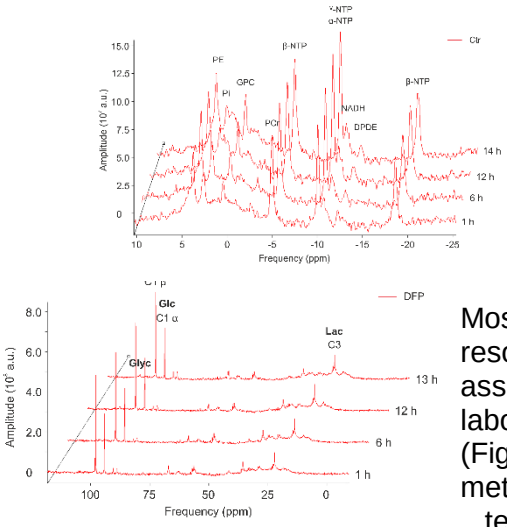

Fig. 1 Top. Serial 31P NMR spectra of 4T1 cells over the courses of 14 hours showing stability of metabolites. Bottom. Serial 13C NMR spectra in cells perfused with 5 mM 1-13C glucose and 100uM DFP.

Due to unanticipated issues with equipment, we have not followed our original experimental plan. Originally, we had anticipated performing the metabolic studies in Year 1 (Aim 1A and 1B) and completing them. These studies were indeed started but as described below, ran into equipment and experimental issues and thus we have focused on performing different parts of the grant proposal in the first year and focused on Aim 2. We think we are poised to readily complete Aims 1,2 in Year 2

1. Metabolic Analyses (Koutcher and Blasberg Lab) (Aim 1)

Most of the time has been invested in trying to get the nuclear magnetic resonance (NMR) perfusion system running in order to perform the metabolic assays on live cells under different experimental conditions in Dr. Koutcher's laboratory. This has been somewhat frustrating but we have things working finally (Fig. 1) studying both 31P (to ensure cell stability) and 13C (intermediary metabolism). The NMR system, the special NMR probe (designed for temperature control, varying exposure to drugs and different conditions), that we had specifically built for these kinds of systems, and the perfusion system itself required extensive repairs and modifications. This is not unusual since it requires a perfectly working complex system

Figure 1 shows a paradigm of an experiment, demonstrating that the system works. We obtained 31P NMR spectra to ensure that the cells are metabolically stable, and serially measure their pH and changes in high energy phosphates, which would drop if the cells were under stress. We then perfuse with 1-13C glucose which allows us to monitor glycolysis and the tricarboxylic acid cycle. We expect in Year 2 to perform the proposed experiments on the MDA-231, 4T1, unpolarized RAW 264.7 cells, and RAW 246.7 cells polarized with interferon and lipopolysaccharides as proposed in the application. Thus we are behind in the metabolic studies of Aim 1 but are ready to perform the experiments

2. Effect of Deferiprone (DFP) Proliferation, migration (Blasberg Lab) (Aim 1)

Our initial studies measuring tumor proliferation showed significant effects of DFP on tumor growth rate in multiple tumor cells. These cells were studied by seeding 50 x10^3 cells in 12 well plates, using drug concentrations of 0, 16, 30, 66, 100, 160, 300, and 660 µM and incubated for 48 hours and evaluated by Trypan Blue assay. Each study was done in triplicate. Since the serum concentrations of DFP after a clinical dose were usually greater than 100uM (1), these data support our hypothesis of the efficacy of DFP in inhibiting tumor growth, in terms of a direct effect on the tumor. We highlighted the two tumor models proposed in our application. In general, the data are consistent with showing an IC50 of between 40 and 65uM in a wide range of cell lines (Table 1). The effect of DFP on enhancing the efficacy of taxol is shown in Table 2 and shows an enhancement of up to 10x in efficacy. The IC50 for cis-platinum was also measured for 4T1 cells and found to be 1.14 +/- 20 uM (mean +/- SD; n=3); studies are ongoing studying the interaction of DFP and cis-platin as proposed. Similar studies on RAW264.7 macrophages (data to date are only on unpolarized cells) showing they also have an IC50 in this range. An IC50 of 72.6 +/- 4.6 uM (mean +/- SD) was measured with an IC90 of 166 +/- 36 uM. Further studies on polarized RAW264.7 cells have just been started and will be reported in Year 2. We anticipate performing studies of the effect of DFP on tumor cell migration in Year 2. Thus the proliferation studies in Aim 1 on the tumor cells are done, leaving the macrophage and migration studies for year 2

Table 1: IC_{50} values for DFP

Cell Lines	IC_{50} (υM)
TRAMP C2	45.7±1.2
MycCaP	48.2±1.2
22rv1	62.3±3.8
MycCaP-CR	52.4±3.4
4T1-WT	40.2±2.6
4T1-NC	39.9±4.1
4T1-KD9	41.6±2.5
E0771	60.6±1.8
MDA-MB-231	58.5±5.6
MDA-MB-231-LM2	64.5±4.3

48h exposure; Mean (SD);

3 independent expts. Cell lines in yellow are TNBC

Table 2: Enhancement of IC50 values for Paclitaxel (nm) in the presence of DFP

Cell line	DFP 0 µM	DFP 50 µM	DFP 100 µM
4T1 (WT)	27.5(7.8)	17.6 (3.2)	3.6(0.3)
4T1-NC	16.6(4.9)	12.4 (1.5)	1.7 (0.5)
4T1-KD9	17.7(7.9)	8.8 (2.4)	1.2(0.1)
E0771	17.4(7.3)	11.6 (2.1)	6.1(1.9)
MDA-MB-231-LM2	6.5(2.2)	1.8 (0.2)	2.4(0.1)
MDA-MB-231	4.9(1.1)	3.8 (0.2)	2.5 (1.4)

Mean (SD); 3 independent triplicate expts

3. Imaging Studies – Non-invasive imaging of changes in macrophage distribution by MR: (**Koutcher Lab**) (2-5);

Gradient echo T_2^* MRI relaxometry was performed to characterize iron in spleen, liver, and mammary tumor in the BALB/c 4T1 model. Deferiprone was administered at 150mg/kg daily until trial endpoint was reached which corresponded to tumor volumes of 60mm^3 as the starting point, and subsequent measurements at 150mm^3, and 500mm^3(end point)

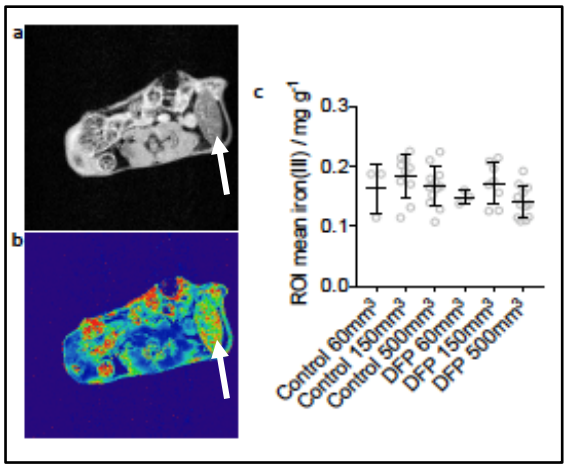

Figure 2. Iron MRI in spleens (arrow) from animals with 4T1 tumors. (a) Gradient echo MRI showing spleen of BALB/c mouse in 4T1 trial (7T body coil, TR/TE 2s/3ms, 0.1mm × 0.1mm × 1mm, 4 averages). (b) Iron map from multi-gradient echo T_2^* MRI showing spleen of BALB/c mouse in 4T1 trial (TR/TE 2s/3ms × 16, 0.1mm × 0.1mm × 1mm, 4 averages). (c) Mean spleen iron value measured from iron MRI maps in control and deferiprone (DFP) treated mice bearing tumors with average sizes of 60mm^3, 150mm^3, and 500mm^3. Points are measurements from individual mice (n=3 60mm^3 control/DFP, n=10 control 150mm^3, n=8 DFP 150mm^3, n=12 control 500mm^3, n=12 DFP 500mm^3). No significant differences are observed according to unpaired students t-test between control and DFP treated groups at similar tumor volumes measurement points. Images in (a) and (b) correspond to measurements made in control mice at 150mm^3 and are representative of all measurement timepoints and treatment groups.

The MRI measurements were conducted at 7T using either a body coil (TR/TE 2s/3ms, 0.1mm × 0.1mm × 1mm, 4 averages) or small coil covering only the mammary tumor (12mm tumor coil, TR/TE 1s/3ms, 0.125mm × 0.125mm × 1mm, 2 averages). Iron level was quantified according to iron calibration curve and mean iron level was measured within region-of-interests drawn over liver, spleen, or mammary tumor (2,3) as we have done previously.

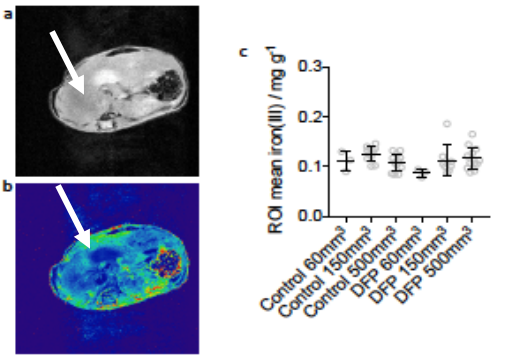

Figure 3. Iron MRI 4T1 model in liver in DFP trial. (a) Gradient echo MRI showing liver of BALB/c mouse in 4T1 trial (7T body coil, TR/TE 2s/3ms, 0.1mm × 0.1mm × 1mm, 4 averages). (b) Iron map from multi-gradient echo T_2^* MRI showing liver of BALB/c mouse in 4T1 trial (TR/TE 2s/3ms × 16, 0.1mm × 0.1mm × 1mm, 4 averages). (c) Mean liver iron value measured from iron MRI maps in control and deferiprone (DFP) treated mice bearing tumors with average sizes of 60mm^3, 150mm^3, and 500mm^3. Points are measurements from individual mice (n=3 60mm^3 control/DFP, n=10 control 150mm^3, n=8 DFP 150mm^3, n=12 control 500mm^3, n=12 DFP 500mm^3). No significant differences are observed according to unpaired students t-test between control and DFP treated groups at similar tumor volumes measurement points. Images in (a) and (b) correspond to measurements made in control mice at 150mm^3 and are representative of all measurement timepoints and treatment groups.

To characterize macrophage iron deposits in the mammary tumors the iron map was stratified in the high-iron range and the pixel cluster analysis tool of ImageJ was used to quantify the total number, size and percent tumor infiltration of high-iron pixel clusters. Figures 2-4 summarize the results from MRI analysis of iron in spleen, liver and mammary tumor (4T1). Overall, iron levels did not vary significantly between measurements made at the various tumor burdens, and deferiprone treatment did not significantly effect the iron levels measured in comparisons between control and treated groups. We hypothesize that this is due to the short period of DFP treatment. Image analysis of mammary tumors for high-iron pixels in Figure 5 revealed few indications of iron deposits across the various cohorts. Most tumors did not contain high-iron pixel clusters within the tumor cross-sections as indicated by the iron MRI scans. When detected, pixel

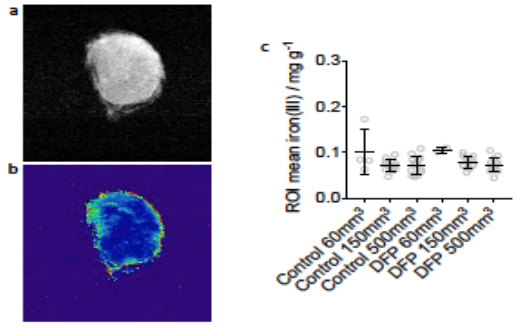

Fig. 4 Iron MRI 4T1 model breast tumor in DFP trial. Note that these data were obtained with the local (tumor coil) and the tumor encompasses the whole field of view. (a) Gradient echo MRI showing breast tumor of BALB/c mouse in 4T1 trial (7T 12mm tumor coil, TR/TE 1s/3ms, 0.125mm × 0.125mm × 1mm, 2 averages). (b) Iron map from multi-gradient echo T_2^* MRI showing breast tumor of BALB/c mouse in 4T1 trial (7T 12mm tumor coil TR/TE 1s/3ms × 16, 0.125mm × 0.125mm × 1mm, 2 averages). (c) Mean breast tumor iron value measured from iron MRI maps in control and deferiprone (DFP) treated mice bearing tumors with average sizes of 60mm^3, 150mm^3, and 500mm^3. Points are measurements from individual mice (n=4 60mm^3 control, n=2 60mm^3 DFP, n=12 control 150mm^3, n=12 DFP 150mm^3, n=13 control 500mm^3, n=15 DFP 500mm^3). No significant differences are observed according to unpaired students t-test between control and DFP treated groups at similar tumor volumes measurement points. Images in (a) and (b) correspond to measurements made in control mice at 150mm^3 and are representative of all measurement timepoints and treatment groups

cluster size corresponded to roughly 1 pixel further indicating sparse accumulation of iron in tumor macrophage of this model, which is different than we have noted in other models and hosts (2,3). A small trend was detected in the number of these high-iron clusters between 150mm^3 and 500mm^3 measurement groups, but statistical analysis of the distributions did not reach significance, and no differences were observed between 150mm^3 and 500mm^3 control and deferiprone treated groups.

Iron deposit accumulation in tumor macrophage as function of percent total ROI of the high-iron clusters was calculated which showed that total area of the high-iron pixels in the tumor cross-sections when detected was approximately 0.1% of total pixels in all cohorts. Plots of the high-iron pixel clusters as a function of % infiltration into the tumors showed that the majority of clusters when detected were found at the outer 10% of the tumor, and no significant differences in this spatial infiltration were observed between cohorts in terms of tumor burden or deferiprone treatment.

To summarize, Aim 2 is significantly complete. The methodology has been developed (2-5), has been evaluated on the 4T1 as proposed, and has also been studied in 2 other breast models (not originally proposed). We undertook the other two models since they were under study as part of a different project and just added the iron analysis. We find that the 4T1 and its host (Balb/C) have significantly less iron than the MMTV breast cancer models (in FVB/N hosts) (4,5). We still need to perform parallel studies on MDA-231 to complete Aim 2

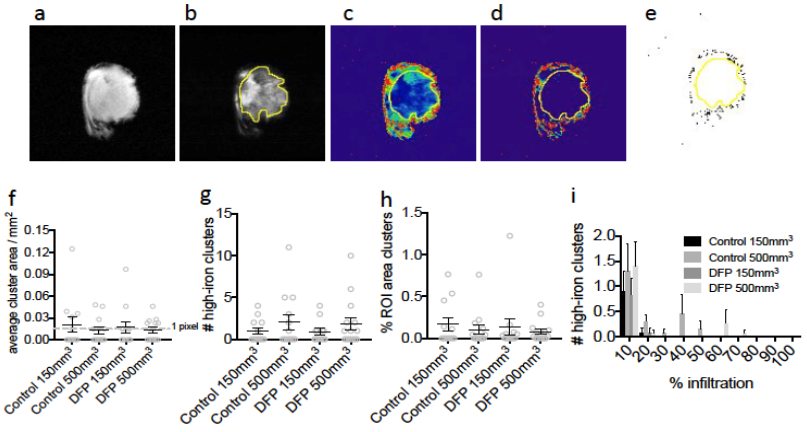

Figure 5. Iron MRI 4T1 model breast tumor high-iron iron cluster quantification in DFP trial. (a) Gradient echo MRI showing breast tumor of BALB/c mouse in 4T1 trial (7T 12mm tumor coil, TR/TE 1s/3ms, 0.125mm × 0.125mm × 1mm, 2 averages). (b) Gradient echo MRI showing breast tumor of BALB/c mouse in 4T1 trial and ROI overlay encompassing tumor (7T 12mm tumor coil, TR/TE 1s/15ms, 0.125mm × 0.125mm × 1mm, 2 averages). (c) Iron map from multi-gradient echo T_2^* MRI showing breast tumor of BALB/c mouse in 4T1 trial showing ROI area (7T 12mm tumor coil TR/TE 1s/3ms, 0.125mm × 0.125mm × 1mm, 2 averages). (d) Stratified iron map (0.15-0.3 mg g^{-1}) from iron map in (c). (e) High-iron pixel clusters identified from (e). (f) Average high-iron cluster area, (g) number of high-iron clusters, (h) percent ROI area of the clusters from iron MRI maps, (i) and percent infiltration into the tumor in control and deferiprone (DFP) treated mice bearing tumors with average sizes of 150mm^3, and 500mm^3. Points are measurements from individual mice (n=12 control 150mm^3, n=12 DFP 150mm^3, n=13 control 500mm^3, n=15 DFP 500mm^3). No significant differences are observed according to unpaired students t-test between control and DFP treated groups at similar tumor volumes measurement points. Images in (a)-(e) and correspond to measurements made in control mice at 150mm^3 and are representative of all measurement timepoints and treatment groups.

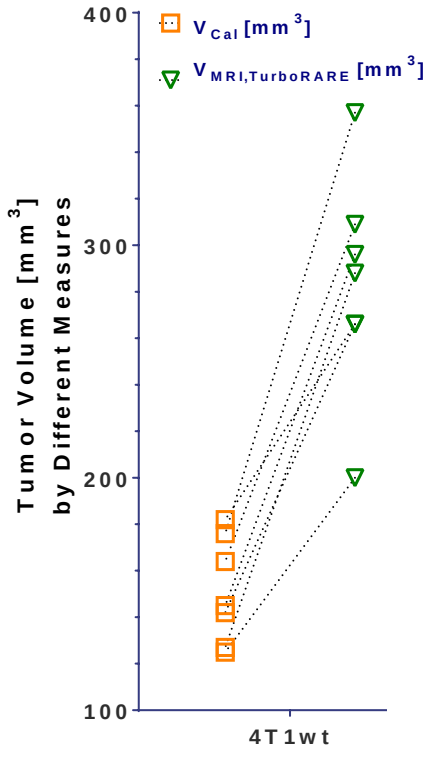

Fig. 6. Effect of measurement by calipers vs MRI. The caliper measurements are inaccurate in measuring tumor depth.

4. Effect of DFP on Tumor Growth/Volume (Blasberg and Koutcher Lab) (Aim 3)

To date, we have performed studies on the 4T1 tumors and are starting to growth the MDA-231 cells for tumor implantation. We have typically measured tumor volumes in breast tumor models by calipers. However, in the 4T1 model we find that it grows deep into the muscle and is

measured poorly by calipers (Ackerstaff E, unpublished, Fig. 6). Fig. 6 shows that tumor volumes measured by calipers are always smaller than measured by MRI. There is wide variation between the caliper and MR measures. Our initial studies with the 4T1 showed an effect on tumor growth with DFP. Using caliper measurements for tumor volume estimation, our data shows significantly more variability which is highly dependent on cohort injection. In 3 cohorts there was a significant decrease in growth rate with DFP which was lost on the fourth one. We ascribe this to variability in estimating tumor sizes by calipers in 4T1 tumors that we have noted grow deeper into the mice, making it impossible to accurately assess tumor volume. We are planning to repeat these experiments measuring tumor volumes 2-3x/week by MRI. This was an unexpected setback costing time and money (mice, imaging time, personnel) but we hope to complete all proposed studies

5. **Flow Cytometry – Effect of DFP on Immune Cells**: (Aim 3) (Blasberg Lab)

Working with Dr. Sadna Budhu from Dr. Merghoub's laboratory, we have investigated the effect of Deferiprone (DFP) on both T cells and macrophages in vivo. These studies on the 4T1 are complete but not analyzed and will be presented in Year 2.

Summary: We have made significant progress in Aim 2, developing the proposed imaging methods and evaluating it on other breast models for comparisons, in addition to the 4T1 as initially proposed. We still need to do the MDA-231 studies. Progress has been slower in Aim 1 although we are not far behind schedule if one considers the sum total.

References

1. Kontoghiorghes GJ, Goddard JG, Bartlett AN, Sheppard L. Pharmacokinetic studies in humans with the oral iron chelator 1,2-dimethyl-3-hydroxypyrid-4-one. Clin Pharmacol Ther. 1990;48(3):255-61. PubMed PMID: 2401124
2. Leftin A, Zhao H, Turkekul M, de Stanchina E, Manova K, Koutcher JA. Iron deposition is associated with differential macrophage infiltration and therapeutic response to iron chelation in prostate cancer. Sci Rep. 2017 Sep 14;7(1):11632. doi: 10.1038/s41598-017-11899-2.
3. Leftin A, Ben-Chetrit N, Klemm F, Joyce JA, Koutcher JA. Iron imaging reveals tumor and metastasis macrophage hemosiderin deposits in breast cancer. PLoS One. 2017 Sep 12;12(9):e0184765. doi: 10.1371/journal.pone.0184765. eCollection 2017.
4. Leftin A, Ben-Chetrit N, Joyce JA, Koutcher JA Imaging endogenous macrophage iron deposits reveals a metabolic biomarker of polarized tumor macrophage infiltration and response to CSF1R breast cancer immunotherapy. Nature Scientific Reports; In Press
5. Avigdor Leftin and Jason A. Koutcher. Quantification of Nanoparticle Enhancement in Polarized Breast Tumor Macrophage Deposits by Spatial Analysis of MRI and Histological Iron Contrast Using Computer Vision. Contrast Media & Molecular Imaging. In Press

Opportunities for Training and Development
Dr. Paola Porcari, a new postdoctoral fellow, is being trained for metabolic studies and has made significant progress. Dr. Leftin, a postdoctoral fellow in the laboratory, has developed the iron MRI imaging methods, validated them histologically and with immunohistochemistry, and is likely to have a faculty position as an outgrowth of these studies. His data has been presented at numerous conferences.

How were the results disseminated:
Dr. Leftin published two papers (Refs 4,5, appendices 1,2) based on support from this grant.

Next Reporting Period Plans to Accomplish Goals:
Major goal is to complete Aim 1 (metabolic studies, proliferation of macrophages). The second major goal would be to perform studies on MDA-231 related to iron imaging (Aim 2) and also response (Aim 3).

At the time of writing our perfusion apparatus is working (Aim 1) and we are purchasing mice for MDA -231 studies

Impact
Nothing to report

Changes/Problems
1. Problems with metabolic studies were discussed above – we do not view this as an issue now
2. We did analyze data on different breast models which was not proposed in the original application. The PI's did not feel this was a major deviation since we did not purchase any mice nor run additional experiments – the data were part of a different study

Products:
Leftin A, Ben-Chetrit N, Joyce JA, Koutcher JA Imaging endogenous macrophage iron deposits reveals a metabolic biomarker of polarized tumor macrophage infiltration and response to CSF1R breast cancer immunotherapy. Nature Scientific Reports; In Press

Avigdor Leftin and Jason A. Koutcher. Quantification of Nanoparticle Enhancement in Polarized Breast Tumor Macrophage Deposits by Spatial Analysis of MRI and Histological Iron Contrast Using Computer Vision. Contrast Media & Molecular Imaging. In Press

Participants:

Jason Koutcher; Corresponding PI, 10% (1.2 months); Dr. Koutcher directs the overall project. Funding Support - NIH

Ronald Blasberg: Supporting PI; 10% (1.2 months); Dr. Blasberg directs/supervises many of the cell studies including oxygen consumption measurements, proliferation etc

Taha Merghoub; Co-investigator (Co-I) 10% (~ 1 month) – supervises flow cytometry and immune studies

Ellen Ackerstaff 10% - (~1 month) (Co-I) Dr. Ackerstaff supervises all the metabolic studies performed both in vivo and in vitro. Other support - NIH

Avigdor Leftin 50% - 6 months Postdoctoral Fellow – Dr. Leftin performs all the iron MRI imaging and the correlative immunohistochemistry and histology. Other support - NIH

Natalia Kruchevsky 50% 6 months. Works with both Dr. Serganova and Dr. Ackerstaff on metabolic studies, measures of tumor cell proliferation and migration. Other support NIH

Sadna Budhu – Co-I – 2.4 calendar months - performs the flow cytometry and immune studies to monitor the effect of DFP on immune cells; Other support - NIH

Inna Serganova – Co-Inv – 1.2 calendar months – Dr. Serganova is a Senior Research Scientist. She supervises Ms. Kruchevsky for the cell proliferation and migration studies and works with Dr. Budhu. Other support – NIH

Jaya Satagopan Co-Investigator – 0.6 months. Dr. Satagopan is responsible for statistical design and analysis of all experiments. Other support - NIH

Changes in Other Support:

Taha Merghoub

(New)

1R01CA227466-01 (PI: Ziv) 7/1/2018 - 6/30/2023 0.60 calendar
NCI $ 68,098
Genetics of Immune Related Adverse Events and Response to Immunotherapy
On this grant, the Memorial Sloan Kettering team (Dr Hellmann) will contribute to overall coordination of the planned research with Dr Ziv, including contributions to study design, data analysis and interpretation, and manuscript preparation.
Role: Collaborator

(New)

MRAP-18-110-01-CCE (PI: Santomasso) 7/1/2018 - 6/30/2020 0.30 calendar
American Cancer Society $ 50,000
Clinical Features and Biomarkers of Immunotherapy Neurologic Toxicity
This application will investigate our central hypothesis that a subset of cancer patients has a baseline autoimmune susceptibility, characterized by a set of pre-existing autoantibodies, that predicts the development and severity of immune-related adverse events (irAEs) after immune checkpoint (IC) inhibition therapy. Validation of this hypothesis would enable clinicians to make treatment decisions earlier, resulting in better management of side effects.
Role: Collaborator

Inna Serganova

(New)

1 R50 CA221810-01A1 (PI: Serganova) 9/5/2018 - 8/31/2023 12.00 calendar
NCI $ 127,102
Exploiting tumor metabolism to optimize T cell therapy
This R50 application (NCI Research Specialist Award; parent R01CA204924; 7/'16-6/'21 "Imaging immune modulation in chimeric antigen receptor (CAR) T cell therapy" and R01CA215136; 7/'17-6/'22 "Imaging tumor and T cell responses to metabolic and immune modulation therapy" requests stable salary support for Dr. Serganova, as she brings unique experience and expertise in reporter systems suitable for PET imaging to monitoring T cell trafficking, activation and persistence non-invasively.
Role: Principal Investigator

No other organizations partnered

Collaborative Award:

This is a collaborative award between Dr. Koutcher and Dr. Blasberg. Note that we have clearly earmarked the contributions of each laboratory

Imaging endogenous macrophage iron deposits reveals a metabolic biomarker of polarized tumor macrophage infiltration and response to CSF1R breast cancer immunotherapy

Authors and affiliations

Avigdor Leftin[1*], Nir Ben-Chetrit[2#], Johanna A. Joyce[2,†], Jason A. Koutcher[1,3]

[1]Department of Medical Physics, Memorial Sloan Kettering Cancer Center, New York, NY 10065, USA

[2]Cancer Biology and Genetics Program, Memorial Sloan Kettering Cancer Center, New York, NY 10065, USA

[3]Department of Medicine, Memorial Sloan Kettering Cancer Center, New York, NY 10065, USA

***Corresponding author:** Avigdor Leftin. Department of Medical Physics, Memorial Sloan Kettering Cancer Center, 1275 York Ave., New York, NY 10065, Phone: 646-888-3469. Fax: 646-888-3476. E-mail: leftina@mskcc.org.

[#]Current address: Nir Ben-Chetrit. Department of Medicine, Weill-Cornell Medical College, New York, NY 10021, USA.

[†]Current address: Johanna A. Joyce. Department of Oncology, Ludwig Institute of Cancer Research, University of Lausanne, CH-1066, Lausanne, Switzerland.

Running title: Macrophage iron imaging in breast cancer immunotherapy

Key words: Breast cancer; CSF1R; immunotherapy; iron; macrophage; MRI.

Abstract

Iron deposits are a phenotypic trait of tumor-associated macrophages (TAMs) that provides for histological and contrast-agent free cellular detection by MRI, but the presence of this biomarker in human cancer, and correlation of this potential metabolic biomarker with immunotherapeutic response is untested. Here, using primarily iron imaging approaches, we evaluated the spatial distribution of polarized macrophage populations containing high endogenous levels of iron in preclinical murine models and human breast cancer, and used them as biomarkers to correlate TAM infiltration with response to immunotherapy in preclinical trials. Macrophage-targeted inhibition of the colony stimulating factor 1 receptor (CSF1R) by immunotherapy was confirmed to inhibit macrophage accumulation and slow mammary tumor growth in mouse models while also reducing hemosiderin iron-laden TAM accumulation as measured by both iron histology and in vivo iron MRI (FeMRI). Spatial profiling of TAM iron deposit infiltration defined regions of maximal accumulation and response to the CSF1R inhibitor, and revealed differences between microenvironments of human cancer according to levels of macrophage iron accumulation in stromal margins. We therefore demonstrate that iron serves as an endogenous metabolic imaging biomarker of TAM infiltration in breast cancer that has high translational potential for evaluation of immunotherapeutic response.

Introduction

Macrophage infiltration is linked to poor clinical outcomes in most cancers such as poor survival, metastatic dissemination, and evasion of anti-tumor immune mechanisms [1-4]. Major efforts are underway to understand the function of macrophage infiltrates in the tumor microenvironment to develop new therapies such as immunotherapies in order to target macrophages and inhibit these deleterious outcomes. To support these efforts there is an increasing need for macrophage biomarkers and imaging approaches that allow for the localization of the targeted macrophage populations according to metabolic phenotype or function which allow measurement of their response to therapy. Histological methods are useful for quantification of macrophage behavior, but in vivo characterization is not possible, and definition of specific phenotypic properties such as polarization status or metabolism can be difficult to generalize from selective biopsy due to tissue intrinsic aspects of macrophage function and the heterogeneous nature of the tumor microenvironment [5, 6]. In vivo approaches such as positron emission tomography (PET) can provide information about tumor macrophage presence, but repeated imaging is limited due to the accumulation of radioactive dose, and resolution of infiltrating macrophages is also limited by current technology [7, 8]. As an in vivo imaging tool, magnetic resonance imaging (MRI) can be used to map many metabolic pathways associated with cancer including glycolysis [9, 10], the tricarboxylic acid cycle [11], phospholipid and ATP metabolism [12, 13], dependencies on perfusion and hypoxia [14], pH [15], and oxidation/reduction balance [16]. Despite this arsenal of anatomical and functional molecular protocols, these non-invasive approaches are usually not able to resolve spatial differences in immune cell metabolism and ascribe them to specific cellular populations within the tumor. This is because the metabolic properties of these populations are often

obscured as they share similar metabolic pathways to the cancer cells, have smaller relative population sizes, and more heterogeneous spatial distributions compared to the bulk of the tumor [17]. Given the available resolution of most metabolic MRI techniques this leads to an average representation of the spatial distribution of metabolites, often reflecting just the dominant cellular population, i.e. the cancer cells, in the metabolic images.

In order to enable the imaging of macrophages according to their metabolic status, we sought to identify metabolic pathways that exhibit higher specificity for these populations rather than cancer cells or other cellular species. Iron metabolism, the processes by which uptake, storage, and re-export of iron takes place, is conserved in most mammalian cells [18]. However, macrophages in particular are known to play a central role in systemic homeostasis of iron according to their unique genetic program that enables them to handle high metabolic flux of this micronutrient [19, 20]. In this iron-regulating role, macrophages can exhibit a unique phenotypic trait, namely the accumulation of aggregates comprised of nanocrystalline iron known as hemosiderin [21]. Recently, we identified endogenous hemosiderin iron deposition as a putative pan-tissue biomarker of TAMs by using clinical iron-sensitive MRI methods (FeMRI) and Prussian blue iron histology without contrast agents to detect accumulated iron in hemosiderin-laden macrophages (HLMs) of murine prostate, breast, and metastatic cancer models [22, 23]. Technically, high-iron concentration FeMRI pixel regions and Prussian blue positive regions indicate the location of macrophage iron deposits that sets them apart from other lower concentration bio-iron sources such as blood due to the physical magnetic and chemical properties of the solid iron stores [24-32]. Similar high-resolution MRI and histological iron imaging approaches can also be used to identify macrophage targets in

cancer but traditionally require intravenous injections of iron nanoparticle contrast agents that rely on macrophage phagocytosis rather than metabolism in a manner similar to many PET probes [33, 34]. However, caveats of the nanoparticle-enhanced MRI and histological techniques include off-target delivery following from the enhanced permeability and retention effect contributed by highly vascularized leaky tumors that reduces specificity for the macrophage deposits [35], and the nanoparticles themselves can induce polarization of macrophages that can potentially bias the metabolic function and the therapeutic response of the targeted populations [36-38]. By recognizing the tendency of macrophages to metabolically accumulate hemosiderin—which generates high-iron contrast akin to that produced using iron nanoparticle injections—microscopic deposits of these cells can be quantified in terms of their abundance and spatial distribution by MRI and histology without contrast agents according to their innate iron metabolism. While these prior studies associated HLMs with TAMs and therefore suggest that they can be used as probes of TAM infiltration to gauge efficacy of immune therapy, here we define the spatial correlations of these metabolically-unique TAM infiltrates with immunotherapy response, and prospectively characterize their distribution in human breast cancer using histological iron imaging in order to support the translation of such combination metabolic iron imaging and therapy approaches to the clinic.

Results

Spatial profiling of tumor macrophage iron deposits with iron imaging

Endogenous FeMRI methods are increasingly favored over the use of invasive biopsy using Prussian blue iron imaging for measurement of non-heme iron concentrations in liver, heart, and brain [25-27, 39-42]. While these methods remove the sampling bias introduced by selective biopsy, they conventionally rely on whole organ averages of cellular iron loading. We rationalized that we could also use FeMRI and correlative Prussian blue histology to detect, resolve, and quantify the spatial distributions of localized TAM iron deposits in breast cancer tumors by addressing spatial heterogeneity of cellular iron deposits through utilization of image analysis algorithms that enable the automatic detection, quantification, and localized mapping of HLM deposits in the iron images. As proof-of-concept, we directly compared histological sections stained for iron using Prussian blue that is specific for HLMs (Figure 1a), with iron maps generated by ex vivo FeMRI-microscopy (Figure 1b) of co-registered tissue sections obtained from an orthotopic TS1 breast cancer model used commonly in TAM research whose tumors are promoted under control of the murine mammary tumor virus which drives expression of the mammary gland specific polyoma virus middle T-antigen (MMTV-PyMT) [43-47]. $Iron^{+}$ TAMs were determined to be the only species to generate distinct high-iron pixel clusters in the MMTV-PyMT tumor cross-sections as comparison of Prussian Blue stained macrophage (Figure 1c) and red blood cells (Figure 1d), another candidate for contributing to iron contrast because of their heme cargo, showed they do not stain for Prussian blue iron and thus contribute only to low FeMRI contrast, further corroborating the specificity of the method for HLMs [22]. We then interrogated the spatial distribution of the HLMs in the histological and FeMRI iron maps as a score of TAM infiltration. Analysis of the histological (Figure 1e), and MRI images (Figure 1f) for high concentrations of iron

yielded maps of the iron containing TAMs. The histological iron deposits and FeMRI pixel clusters were then graphed as a function of position in the tumor (% infiltration, Figure 1g), and the radial infiltration profiles of the histological deposits and MRI clusters were found to be the same (Figure 1h, $p>0.05$). This confirmed the equivalence between the HLM measurements by FeMRI and histology, and further provided a novel means to map the spatial distribution of the HLM deposits according to metabolic status with cellular sensitivity.

Correlation between immunotherapeutic CSF1R inhibitor response and polarized iron deposit accumulation.

To then further establish these TAM iron deposits as immunotherapy targets, we initiated preclinical CSF1R (colony-stimulating factor-1 receptor) inhibitor (BLZ945) trials in murine breast cancer models. This receptor kinase inhibitor blocks the interaction between the cytokine colony stimulating factor 1 (CSF1) that mediates macrophage accumulation in tumors via signaling with its receptor CSF1R [48, 49]. The drug has been shown to have the primary immune effect of inhibiting the accumulation of TAMs in tumors, making it an excellent candidate for testing the iron imaging approaches, and it has the coincident therapeutic effect of slowing the growth of breast, cervical, brain, and other cancers [46, 50-53]. Cell-line derived TS1 and 99LN MMTV-PyMT tumors orthotopically implanted in the mammary fat pads of their respective syngeneic FVB/N and C57BL6 hosts were studied. Treatment with the small molecule CSF1R inhibitor BLZ945 was initiated when tumors reached approximately $100mm^3$ in the TS1 and 99LN models. Treatment continued until control tumors reached or exceeded $1cm^3$ measured by caliper to establish

pre-treatment and endpoint imaging time points, and significant tumor growth inhibition was observed in both models with CSF1R inhibition by these endpoints (Figure 2a, $p<0.001$-$p<0.0001$). Subsequent measurement of the tumor volumes made by MRI in the imaging studies of the control and BLZ945 treated TS1 (Figure 2b-2c) and 99LN models (Figure 2d-2e) recapitulated the reductions in tumor volumes established by the initial pilot trials where TS1 tumor volumes were 51% of controls, and the drug also limited the growth of the 99LN model tumors to approximately 34% of the untreated groups (Figure 2f, $p<0.01$).

To then characterize the primary inhibitory effect of the CSF1R inhibitor on TAM accumulation as has been done in previous studies in MMTV-PyMT models with the BLZ945 drug and others [43, 46], whole tumors from the TS1 and 99LN models were collected at imaging endpoints and single-cell suspensions were prepared from the homogenates. Fluorescence staining of the cells for live $CD45^{+}Ly6c^{-}Ly6g^{-}CD11b^{+}F4/80^{+}$ TAMs was then performed and the frequency of these cells was quantified by flow cytometry. Treatment with BLZ945 reduced the frequency of TS1 TAMs (Figure 2g-2h), and similarly 99LN models also exhibited reductions in TAMs (Figure 2i-2j) in accord with the previous studies of the inhibitor, thereby providing further preclinical validation for our imaging studies. Overall the CSF1R immune therapy lowered the frequency of TAMs with respect to total $CD45^{+}$ cells in the tumors significantly with levels of BLZ945 treated TAM fraction by approximately 30% of the control levels in both TS1 and 99LN groups (Figure 2k, $p<0.001$- $p<0.01$).

In order to quantify the response of $iron^{+}$ TAMs to the BLZ945 inhibitor, we performed Prussian blue histology specific for the TAM iron deposits beside CD68

macrophage histology as a general marker of TAMs. First, digitized images of paraffin-embedded whole axial cross-sections of the tumor collected at CSF1R trial endpoints were analyzed by counting all TAMs according to their CD68 staining to measure general response to the CSF1R inhibitor. Reduced numbers of $CD68^+$ infiltrating macrophages were found in both the TS1 (Figure 3a-3b) and 99LN cohorts (Figure 3c-3d) confirming previous studies of this inhibitors effects on TAM accumulation in MMTV-PyMT models [43]. Overall, $CD68^+$ macrophages were lower by approximately 42% in the TS1 model and 55% in the 99LN model following BLZ945 treatment (Figure 3e, $p<0.01$) generally recapitulating the reductions in TAMs measured by flow cytometry in the trials. Histological assessments of HLMs using Prussian blue iron staining were performed in the same manner as CD68 histology. TS1 tumors in the syngeneic FVB/N background exhibited numerous HLM deposits consisting of colonies of $iron^+$ TAMs found largely in stromal margins of the paraffin embedded tumor cross-sections (Figure 3f), and treatment with BLZ945 reduced the number of these cellular species (Figure 3g). The $iron^+$ TAMs were relatively fewer in the 99LN models, but were still detected in the digital image analysis of the Prussian blue iron-stained 99LN tumors (Figure 3h), and these iron deposits were also lowered with BLZ945 treatment (Figure 3i). Administration of the CSF1R inhibitor reduced $iron^+$ TAM accumulation by approximately 50% in the TS1 models and 85% in the 99LN models (Figure 3j, $p<0.001$), again corroborating the primary effect of the CSF1R inhibitor on TAM accumulation, and further indicating that this drug also effects iron containing TAM populations.

Macrophage accumulation in tumors fulfills both inflammatory and anti-inflammatory roles, but little is known about the polarization and CSF1R status of $iron^+$

TAMs. To investigate the polarization status of these macrophage subpopulations, Prussian blue iron-stained histological sections (Figure 4a, 4b) were re-stained using multiplexed immunofluorescence for M1-like (Figure 4c, 4d, pro-inflammatory, AIF1; allograft inflammatory factor-1), M2-like (Figure 4e, 4f, anti-inflammatory, CD206; mannose receptor), and CSF1R receptor (Figure 4g, 4h) markers in the TS1 and 99LN models. Controlling for the primary inhibitory effect on the accumulation of $iron^+$ populations, fields containing the $iron^+$ TAMs in control tumors and fields still containing iron deposits following BLZ945 treatment were identified in the registered tumor cross-sections in order to quantify the co-positivity of the $iron^+$ TAMs as a function of M1-like, M2-like, and CSF1R status in these localized regions. Counts of these macrophage populations in the TS1 and 99LN tumors (Figure 4k, 4l) showed that TS1 tumors had relatively higher numbers of macrophages expressing polarization markers and CSF1R compared with the 99LN model in accord with the cell counts made independently of polarization status. The CSF1R inhibitor BLZ945 did not greatly effect these general populations, though a small reduction of $CD206^+$ macrophage was observed in the TS1 deposit regions ($p<0.05$). To specifically assess changes in polarization status of the $iron^+$ macrophages with BLZ945 treatment, the fractions of $iron^+$ macrophage subpopulations expressing M1-like, M2-like, and mixed M1- and M2-like markers were calculated as a function of the total $iron^+AIF1^+$, $iron^+CD206^+$ and $iron^+AIF1^+C2206^+$ populations in the TS1 (Figure 4m) and 99LN models (Figure 4n). Similarly, the $iron^+AIF1^+$, $iron^+CD206^+$ and $iron^+AIF1^+CD206^+$ populations were also assessed for CSF1R positivity calculated as a fraction of total $iron^+CSF1R^+AIF1^+$, $iron^+CSF1R^+CD206^+$ and $iron^+CSF1R^+AIF1^+CD206^+$ macrophages present (Figures 4o, 4p). This analysis revealed that while the $iron^+$ populations were found

co-localized with AIF1 and CD206 polarization markers as well as CSF1R, the fraction of these iron$^+$ M1-like and iron$^+$ M2-like species and their CSF1R$^+$ counterparts in these iron deposit regions were largely unaffected by the CSF1R inhibitor except for small differences in iron$^+$AIF1$^+$CD206$^+$, iron$^+$CSF1R$^+$AIF1$^+$ and iron$^+$CSF1R$^+$AIF1$^+$ CD206$^+$ populations in the fields assessed ($p<0.05$). This histological analysis indicates that polarization of the iron$^+$ populations, and general populations overall is largely unaffected by the CSF1R inhibitor, and also indicated that the HLMs were not significantly biased towards a given polarization state as they were frequently co-localized with multiple markers.

Iron imaging of macrophage tumor infiltration in CSF1R inhibitor trials

In vivo contrast-agent free FeMRI was then used to quantify macrophage iron deposits of the MMTV-PyMT models in the BLZ945 trials, and correlate their detection with the CSF1R inhibitor's primary immunotherapeutic effects on macrophage accumulation and tumor growth. FeMRI images were quantified using image-processing algorithms demonstrated above in the ex vivo analysis. Control and BLZ945 treated MMTV-PyMT mammary tumors exhibited high-iron pixel clusters indicative of macrophage iron deposits in both the TS1 (Figure 5a-5b) and 99LN (Figure 5c-5d) models. High-iron pixel clusters found in BLZ945 treated tumors were approximately 37% of control levels in both models (Figure 5e $p<0.01$) supporting the flow cytometry and histological measurements as shown in Figures 2 and 3. Tumor growth and accumulation of FeMRI clusters were positively correlated in both TS1 (Figure 5f) and 99LN models

(Figure 5g), and immunotherapeutic response was indicated by a reduction in tumor growth and inhibition of FeMRI cluster accumulation.

Counts of the high-iron FeMRI pixel clusters and HLM deposits found in histological Prussian blue iron images were also analyzed as a function of position in order to establish spatially-resolved scores of immunotherapeutic response (Figure 6a-6d). The scores of the FeMRI clusters (Figure 6e-6f) and HLM deposits (Figure 6g-6h) both showed higher levels of TAMs at the stromal margins of the tumors with decreasing numbers of iron containing cells found towards the tumor core where less macrophage infiltration generally occurs. Treatment with BLZ945 resulted in overall lower levels of the iron containing regions throughout the tumor cross-sections, and the infiltrating clusters measured by FeMRI and HLM deposits measured by Prussian blue histology at the outer margins of the tumors were most affected by the CSF1R therapy as indicated by their significant reductions ($p<0.05$-$p<0.0001$). This establishes that contrast-agent free in vivo FeMRI can detect and map macrophage iron deposits in a similar manner to ex vivo iron histology, and that using FeMRI and iron histology during CSF1R immunotherapy provides measurements of TAM infiltration correlated with the regions of maximal immunotherapeutic response. Thus, iron serves as a novel biomarker indicating response to immunotherapy treatment that can be monitored in vivo using non-invasive MRI technology.

Prospective survey of polarized macrophage iron deposit infiltration in human breast cancer

The eventual clinical translation of iron as a biomarker for macrophage detection and its combination with CSF1R immunotherapy largely depends on whether iron deposits are detectable in human breast cancer. Therefore, prospective surveys of histological samples containing regions of human carcinoma in situ and invasive carcinoma were performed by staining the paraffin-embedded sections with the Prussian blue method to identify non-heme iron deposits specific to HLMs. Iron deposits were detected in the stromal margins of carcinoma in situ (CIS, Figure 7a), and were also detected at stromal boundaries of invasive carcinoma (INV, Figure 7b). In regions densely populated by cancer cells in highly invasive carcinoma where stromal margins were not evident these deposits were absent (Figure 7c). Profiling of HLM deposit infiltration as a function of position across regions indicative of CIS (Figure 7d) and INV where the HLMS are present (Figure 7e) further indicated significant spatial differences between the HLMs in these breast cancer microenvironments. Similar to the murine spatial infiltration profiles, human HLMs were more abundant at the outer stromal margins of the tumors, and in situ carcinoma was found to exhibit higher numbers of infiltrating HLMs compared with the margins of the invasive carcinoma tumor microenvironments (Figure 7f, $p<0.01$-$p<0.0001$). This confirmed the association of macrophage iron deposits with human breast cancer, and shows that while they are commonly found in the tumor-stroma boundaries of both cancer subtypes they are more prominently observed in the in situ pathologies where the stromal margins are better defined compared to invasive carcinoma where such margins can be less evident. As in situ carcinoma is thought to precede the emergence of invasive carcinoma, these findings support the translational value of using iron as an early cancer imaging biomarker of TAMs.

The iron$^+$ TAMs in the human cancers were further tested for polarization and CSF1R status using multiplexed immunofluorescence imaging methods as we performed in the murine CSF1R inhibitor trials [54]. The CIS and INV fields stained for Prussian blue iron$^+$ HLMs (Figure 8a,8b) were re-stained for inflammatory M1-like macrophages (Figure 8c,8d; AIF1), anti-inflammatory M2-like macrophages (Figure 8e,8f; CD206), and the CSF1R receptor (Figure 8g,8h) in order to determine the co-positivity of iron with these markers (Figure 8i,8j). The total numbers of macrophages were assessed in fields centered on HLM deposits in the stromal margins of the CIS and INV regions. The AIF1$^+$, CSF1R$^+$, and CD206$^+$ macrophages were significantly different in the CIS and INV regions (Figure 8k) and corresponded to higher numbers of pro-inflammatory AIF1$^+$ cells in INV fields ($p<0.0001$), while CSF1R$^+$ ($p<0.05$), CD206$^+$ ($p<0.01$), and iron$^+$ macrophages ($p<0.001$) were significantly lower in these same regions. To quantify the association of the iron$^+$ macrophages with these markers the fraction of iron$^+$AIF1$^+$, iron$^+$CD206$^+$, iron$^+$AIF1$^+$CD206$^+$ macrophage were calculated as a function of the total polarized iron$^+$ TAM population (Figure 8l), and similarly these iron$^+$ populations were assessed for co-positivity with the CSF1R marker (Figure 8m) to determine whether the iron$^+$ TAMs in these fields express this receptor to further motivate later immunotherapeutic interventions using CSF1R inhibitors. Overall, significantly higher fractions of iron$^+$AIF1$^+$ ($p<0.01$) and iron$^+$AIF1$^+$CD206$^+$ ($p<0.0001$) macrophages were found in CIS microenvironments while iron$^+$CD206$^+$ markers were statistically the same in CIS and INV locations. Additionally, the calculation of the fraction of the iron$^+$AIF1$^+$ and iron$^+$CD206$^+$ populations with CSF1R indicated that significantly more iron$^+$CSF1R$^+$AIF1$^+$ ($p<0.001$) and iron$^+$CSF1R$^+$CD206$^+$ ($p<0.001$) macrophages were present in CIS fields and iron$^+$CSF1R$^+$AIF1$^+$CD206$^+$

populations were largely the same in the CIS and INV microenvironments. Thus, we demonstrate that TAMs in the human breast cancer microenvironments differ in their phenotype, and that iron accumulation occurs in polarized TAMs of human breast cancer. Interestingly, the iron$^+$ macrophages in both cancer types were associated with polarization markers as well as CSF1R while the fraction of these polarized iron$^+$ subpopulations was biased towards M1-like and CSF1R$^+$ status in the CIS regions, but also frequently exhibited mixed phenotypic character in both settings. In the context of our novel iron imaging approaches, this indicates that while macrophage polarization is an important immunological factor in both murine and human cancers, the number of iron$^+$ macrophages itself can serve as a TAM imaging biomarker that is sensitive to microenvironment and stage of the cancer with high-potential for in vivo detection by MRI.

Discussion

The accumulation of hemosiderin iron in tumor-associated macrophages enables the imaging of these cells in heterogeneous tumor microenvironments according to localized differences in iron metabolism. In earlier studies we reported that iron-deposits occur in the stromal margins of murine mammary tumors and prostate cancers using histological imaging and in vivo FeMRI [22, 23]. Recently, these iron deposits have also been detected in the stromal margins of non-small cell lung cancer tumors [36], and we have also shown them to be present in lung and brain metastases [22]. In the current study we confirmed that such TAM iron deposits are present in multiple MMTV-PyMT breast cancer models, they are correlated with response to CSF1R breast cancer immunotherapy, and we demonstrated that the spatial infiltration and accumulation of the TAM iron

deposits is a factor that is conserved in murine and human breast cancer and differentiates between human breast cancer microenvironments.

From an in vivo imaging standpoint our novel measurements also serve to further establish FeMRI as a unique approach for the detection and monitoring of immune cells with potential utility for monitoring cellular response to cancer immunotherapy. Alternative MRI approaches label macrophages using injections of iron nanoparticles [33, 34, 55], and injected radiolabelled nanoparticles used in PET imaging can also be used to measure macrophage during immunotherapy trials [8, 56]. Our imaging studies are set-apart from these contrast agent-dependent techniques as we do not use contrast agent injections. We instead capitalize on the physiological innate iron metabolism of macrophages that results in the phenotypic storage of solid deposits of iron that is readily validated using Prussian blue iron histochemistry of the TAM iron deposits. These magnetic deposits give rise to characteristic high-iron FeMRI pixel contrast that reveals their infiltration in micro-hemorrhagic environments where they fulfill obligate roles in iron storage and recycling [20, 30, 57]. Although our reliance on endogenous iron stores to image TAMs is potentially restricted because we only detect those macrophages engaged in iron handling roles, the current findings showing HLMs in the different MMTV-PyMT backgrounds as well as human cancers support the feasibility of using the iron imaging approaches to image them and supports the combination of this form of endogenous cell-tracking with immunotherapeutic trials targeting macrophage in the clinic.

While we focus on iron as a primary biomarker of tumor macrophages in this contribution, TAMs are also recognized to adopt so-called polarization phenotypes that are closely associated with their role in immune response and communication to other immune

cells such as T-cells that is critical for immunotherapeutic efficacy [46, 51]. These multifactorial polarization states reflect the stage of immune response, progression of primary tumor and metastasis growth, as well as the microenvironment and tissue in which they are found [6]. We discovered that macrophage iron deposits are found more prevalently at the stromal margins of tumors in murine models and human breast cancers suggesting that iron is another microenvironmental factor influencing macrophage phenotype and spatial distribution. However, when we investigated the polarization status of the macrophage iron deposits we found them to be associated with various phenotypic polarization markers, and they were often co-localized with macrophage markers indicating mixed polarization character, rather than adopting a single polarization state. While the current studies do not address the functional significance of such polarization states in the context of their role in signaling to other immune cells, it is evident due to their clear association with iron that they serve a primary functional role in iron metabolism. In this regard it can be speculated that iron$^+$ macrophages are primed to fill M1-like inflammatory functions where they sequester iron to shield it from depletion due to hemorrhage or pathogen, as well as function in M2-like wound-healing roles where they serve as stores of iron to sustain cellular proliferation of the microenvironmental milieu during tissue repair [58]. This scenario is supported by our observations of the differences in iron$^+$ macrophage of in situ and invasive human cancers. Here, more iron$^+$ macrophages were found in earlier cancer stages suggesting that these macrophages avidly stored iron during initial inflammatory immune response to the cancer. Similarly, in advanced cancers reduced numbers of iron-containing TAMs presumably reflects the depletion of stromal macrophage iron stores in order to fuel the cancer's malignant outgrowth as it has been

proposed that cancer cells have a pronounced dependence on iron metabolism that serves to co-opt this critical micronutrient from other cellular species in the tumor microenvironment [59, 60]. In this context, the iron^{+} deposits can themselves be used as specific histological and in vivo biomarkers of TAM infiltration which varies with immune status and cancer stage without the need for assessment of tissue-dependent polarization.

Immune therapies such as the small molecule inhibitors of macrophage colony stimulating factor 1 receptor (CSF-1R) including BLZ945 and PLX3397, as well as antibodies directed against this receptor have been shown to reduce the accumulation of TAMs in preclinical models to achieve therapeutic gains as monotherapy and in combination with other therapies [46, 50]. We confirmed the primary immunotherapeutic effects of the CSF1R inhibitor in the MMTV-PyMT mammary tumor models by demonstrating that the drug achieves reduction in macrophage accumulation together with tumor growth inhibition. We also confirmed that the iron^{+} macrophages express CSF1R in murine and human breast cancers supporting their role as targets of these immunotherapies. Indeed, inhibition of macrophage accumulation by CSF1R therapy resulted in significant reductions of iron-laden macrophage deposits in the orthotopic MMTV-PyMT models. Therefore, these studies validated the immunotherapeutic effect of the drug in the breast tumor models, further identified the iron-laden macrophage populations as responsive to the CSF1R immunotherapy, and confirm their CSF1R status for future therapeutic targeting in human cancer.

Cancer therapies targeting iron metabolism under current investigation have sought to either achieve therapeutic gains by iron loading using nanoparticle injections, or by causing iron depletion with iron chelators [23, 36, 38, 61]. In the current studies we identify

another means of targeting cellular iron for therapy. By capitalizing on the observation that iron deposits are restricted to TAMs, we demonstrate that CSF1R inhibition that directly targets TAMs can also be used to indirectly prevent accumulation of TAM iron deposits. As our murine investigations and surveys of human breast cancers indicate the presence of these cells and indicate they follow characteristic spatial dependencies, the detection of these iron deposits, targeting the iron deposits using CSF1R inhibitors, and spatially monitoring them using iron imaging has notable value in cancer therapy and potentially other diseases such as iron overload disorder, neurodegeneration, inflammation, and hemorrhage where iron deposits may be present and their detection, mapping, and subsequent therapeutic reduction can be desirable [39, 40, 57, 62] .

Conclusions

In sum we identified metabolic iron deposition as a biomarker of macrophage infiltration in murine and human breast cancer that identifies responsive TAM populations to CSF1R immunotherapy using histological and in vivo iron imaging together with preclinical cancer research approaches. While the current studies support our ability to image polarized TAMs according to iron status in breast cancer, and suggests that iron deposits are associated with specific types of cancer, given the diverse types of human breast cancers encountered in the clinic further histopathology will be required to more completely characterize the association of the deposits with the myriad immunological markers involved in immunotherapeutic studies, as well as correlate their accumulation with cancer stage, and clinical outcome. Also, though these findings support the translation of the FeMRI approaches to human breast cancer, and our detection of iron deposits in

human cancer strongly supports the feasibility of this approach, further imaging validations will ultimately determine whether the approaches presented here will find their niche in clinical cancer imaging and immunotherapy trials in the future. Therefore, these proof-of-concept demonstrations support such future studies that seek to image immune cells and harness their innate functional and metabolic dependencies for cancer therapy.

Acknowledgments. We thank Marion Wiesmann (Novartis) for providing the CSF1R inhibitor BLZ945 and review of the manuscript. We also thank Dr. Katia Manova-Todorova, Dr. Dmitry Yarilin, Dr. Sho Fujisawa, and Dr. Mesruh Turkekul of The Molecular Cytology Core Facility at Memorial Sloan Kettering Cancer Center for discussions, histological processing services and instruction, and research tissue samples. Funding support is acknowledged from NIH grants PO1 CA115675, DOD BC161705 and P30 CA008748 (Cancer Center Support Grants), Breast and Molecular Imaging Fund at MSKCC Evelyn H. Lauder Breast Center, NCI 1F32CA206277, and the Breast Cancer Research Foundation.

Author Contributions: A.L. designed the study. A.L. collected MRI and histological data, and performed MRI and histological analysis. A.L. and N.B.C. initiated and maintained mouse models. A.L. and N.B.C. collected and analyzed FACS data. A.L. wrote the paper, and A.L., N.B.C., J.A.J., and J.A.K. edited and approved the paper.

Competing Interests: None

Methods

Magnetic resonance imaging. MRI was performed on a 7T/30 cm horizontal bore Bruker Biospec MRI system (Bruker Biospin Corp.) with a custom-built 30 mm inner-diameter transmit-receive quadrature radio-frequency coil.

Iron MRI. 2D multi-gradient echo (MGE) relaxometry pulse sequence was used with the following parameters: TR/TE 1.2s/3ms×16 echos, in vivo spatial resolution 0.1mm×0.1mm×1mm, ex vivo 0.05mm×0.05mm×0.5mm, RF flip angle 60°, and each spatial encoding phase encode acquisition was gated on the animal's respiratory cycle. The first image of the gradient-echo series was used as reference images shown in the figures and overlays.

Aqueous solutions of iron(III) nitrate (Fisher Scientific) were used as standards for iron concentration measured at 7T as described in refs [22, 23]. Briefly, the T_2^* values for these solutions was determined by pixel-wise monoexponential fitting of the MGE images using Fiji [63]. A linear relation between the relaxation rate $R_2^*=1/T_2^*$ and known iron concentrations was found, and was subsequently used to generate parametric maps of iron concentration. Quantification of FeMRI clusters was conducted by binary stratification of the concentration range of the iron maps (total range, 0.0-0.3 mg g^{-1}; high, 0.15-0.3 mg g^{-1}) followed by counting the frequency of the high-iron pixel clusters with the Fiji Analyze Cluster tool. Infiltration profiles of the high-iron clusters were generated by measuring them as a function of position according to a concentric ring pattern generated with the Fiji ROI Manager tool macros.

Animal procedures. All animal studies were approved by the MSKCC IACUC committee and performed in accordance with their guidance and regulations.

In vivo MRI. Mice were anesthetized with 1-3% isoflurane in O_2 gas, and respiration was monitored during all imaging sessions.

Primary tumor models. Female 6 week-old FVB/N or C57BL6 mice underwent orthotopic mammary fat pad injection of injection of 1×10^6 syngeneic TS1 MMTV-PyMT or 99LN tumor cell lines grown and collected using standard tissue culture conditions and suspended in a 50% solution of Matrigel and saline (BD Bioscience). Endpoint was defined as when the control cohorts average tumor size reached approximately $1cm^3$ determined by caliper, MRI, or veterinary staff inspection notice.

CSF1R inhibitor administration. The CSF1R inhibitor BLZ945 (Novartis) was administered by oral gavage (200 mg kg^{-1} in captisol vehicle, 5x/week). Dosing commenced once tumors exceeded approximately 100 mm^3 and continued until control cohorts average tumor size reached approximately $1cm^3$ determined by caliper, MRI, or veterinary staff inspection notice.

Flow cytometry. Tumor-bearing mice at endpoint were perfused with 20mL of PBS prior to mammary tumor retrieval at endpoint. Tumors were washed once in PBS and enzymatically digested for 45 min into a single cell suspension using a tumor dissociation kit (Miltenyi Biotec). Cell suspensions were filtered twice through 70μm cell strainers, and Fc-blocked for 30 min on ice (1:50; clone 2.4G2, BD Bioscience). Cells were then immunostained using antibodies (BioLegend) for CD45 (1:400; clone: 30-F11), Ly-6C (1:400; clone HK1.4), Ly-6G (1:400; clone 1A8), CD11b (1:200; clone M1/70), and F4/80 (1:250; clone BM8) for 45 min on ice. Cells were then washed twice in PBS and suspended

in FACS-buffer (2% FBS in PBS) containing DAPI (2.5□g/mL; Invitrogen) for exclusion of dead cells. TAMs were identified as $DAPI^{-}CD45^{+}Ly6C^{-}Ly6G^{-}CD11b^{+}F4/80^{+}$ cells, and frequency of TAMs was determined from counts in the $F4/80^{+}CD11b^{+}$ flow cytometry gates with respect to total live $CD45^{+}$ cells using FCS Express.

Histology. Cross-sections from the PBS-perfused MMTV-PyMT tumors were sliced at the axial tumor midpoint and fixed in 4% PFA for 24 hours at 4 ^{0}C, and then washed with H_2O and re-suspended in 70% ethanol (Fisher Scientific). Human tissue sections donated to the Molecular Cytology Core Facility by the Pathology Department were acquired under MSKCC Institutional Review Board informed consent and provided for the study without any unique patient identifiers except diagnosis. They were fixed in 10% neutral buffered formalin. All tissues were paraffin embedded and 5μm sections cut onto glass slides for histology.

The Prussian blue histochemical detection of iron(III) was performed by first manually de-paraffinizing in xylene, and re-hydration in series of alcohol dilutions (100%, 95% and 70%) and tap water. Slides were then placed in a working solution of equal parts 10% potassium ferricyanide (Fisher Scientific) and 10% hydrochloric acid (Fisher Scientific) prepared in distilled water and stained for 30 minutes. Slides were rinsed in distilled water, counter-stained with nuclear-fast red for 30 minutes and cover-slipped with Permount (Fisher Scientific).

The immunofluorescent detection of CD68 was performed using a Discovery XT processor (Ventana Medical Systems). The tissue sections were de-paraffinized with EZPrep buffer (Ventana Medical Systems), antigen retrieval was performed with CC1 buffer (Ventana Medical Systems), and sections were blocked for 30 minutes with

Background Buster solution (Innovex) followed by Avidin/biotin blocking for 8 minutes. CD68 (Boster, cat# PA1518, 5ug/ml) was applied and sections were incubated for 5 hours followed by 60 minutes incubation with biotinylated goat anti-rabbit antibodies (Vector Labs, cat#PK6101) at 1:200 dilution. The detection was performed with Streptavidin-HRP D (part of DABMap kit, Ventana Medical Systems) followed by incubation with Tyramide Alexa Fluor A546 (Invitrogen, cat# T20933) prepared according to manufacturer's instructions with predetermined dilutions. After staining slides were counterstained with DAPI (Sigma Aldrich, cat# D9542, 5 μg/ml) for 10 min and coverslipped with Mowiol.

Multiplex immunofluorescent stainings were performed as previously described [54]. Prussian blue stained slides were de-coverslipped, rehydrated and differentiated, and sections were then sequentially incubated with anti-CSF1R (Santa Cruz, cat#sc-692, 0.5μg/ml) for 5 hours followed by 60 minutes incubation with biotinylated goat anti-rabbit IgG (Vector labs, cat#PK6101) at 1:200 dilution, anti-CD206 (Abcam, cat#ab64693, 1μg/ml) for 5 hours followed by 60 minutes incubation with biotinylated goat anti-rabbit IgG (Vector labs, cat#PK6101) at 1:200 dilution, and finally anti-AIF1 (Wako, cat#019-19741, 0.5μg/ml) for 5 hours followed by 60 minutes incubation with biotinylated goat anti- rabbit IgG (Vector labs, cat#PK6101) at 1:200 dilution. The detection was performed successively for each of the antibodies using streptavidin-HRP D (part of DABMap kit, Ventana Medical Systems) followed by incubation with Tyramide Alexa 488 (Invitrogen, cat# B40953) for CSF1R, Tyramide Alexa 647 (Invitrogen, cat# B40958) for CD206, and Tyramide Alexa 568 (Invitrogen, cat# T20948) for AIF1 prepared according to manufacturer instruction with predetermined dilutions. After staining slides were

counterstained with DAPI (Sigma Aldrich, cat# D9542, 5 µg/ml) for 10 min and coverslipped with Mowiol.

Histological sections were digitized with a Mirax scan system and read with Panoramic Viewer (3DHISTECH, Budapest Hungary). Images were first visually inspected for quality and then processed to remove background fluorescence and provide maximal signal for binary spot counting performed over whole cross-sections or selected fields from exported images using Fiji. Cells were quantified by image thresholding according to staining or immunofluorescent labeling. Iron$^+$ macrophages were identified by thresholding according to their blue color, and immunofluorescent positive macrophages were identified by their respective immunofluorescent colors. Deposits of iron containing macrophages were identified by processing the Prussian Blue histology using the Fiji Analyze Cluster tool as described in ref [22]. Briefly, iron deposit maps were generated by resizing the histological images by using pixel averaging and bilinear interpolation to down-sample the iron image mask size to the resolution of the MRI experiment. The resulting binary deposit maps were then processed by watershed gradient, and finally the frequency of the deposits was determined using the Fiji Analyze Cluster tool. Infiltration profiles of the iron deposits were evaluated by counting them as a function of position in the tumor cross-section using a concentric sampling pattern generated with the Fiji ROI Manager macro tools. Evaluation of iron$^+$ macrophage phenotype in murine and human tissue was conducted by co-registering Prussian blue and triple-stained immunofluorescent images, identification of 200µm×200µm fields centered on iron deposits, and performing exhaustive binary counts made of the iron$^+$ cells as a function of AIF, CD206 and CSF1R positivity in Fiji. Fractional populations were calculated by

dividing the total counts of a given set of co-localized macrophage markers by the sum of the markers being compared, for example M2-like polarization of iron containing macrophage was calculated by dividing the $iron^{+}CD206^{+}$ population by the sum of $iron^{+}AIF1^{+}$, $iron^{+}CD206^{+}$, and $iron^{+}AIF1^{+}CD206^{+}$ populations.

Statistics. Statistical calculations are indicated in the figure legends when performed and significance is determined as $p<0.05$ in all analyses. All statistical analyses were performed with GraphPad Prism 7 (GraphPad Software).

Figures

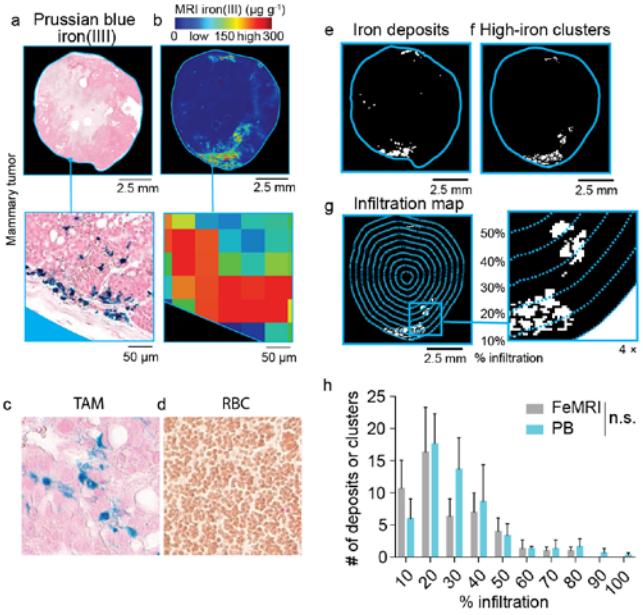

Figure 1. Imaging and spatial profiling of tumor macrophage iron deposits ex vivo with iron MRI (FeMRI) and Prussian blue iron histology. (a) Representative Prussian blue iron histology of MMTV-PyMT TS1 mammary tumor cross-section. Scale bar 2.5mm. Expansion shows iron$^+$ macrophage deposits. Expansion scale bar 50μm. (b) Representative ex vivo FeMRI of MMTV-PyMT TS1 mammary tumor cross-section. Scale bar 2.5mm. Expansion shows high-iron pixel clusters. Expansion scale bar 50μm. (c) Representative Prussian Blue iron histology of tumor associated macrophages (TAM), and (d) red blood cells (RBC). Note iron$^+$ macrophages and iron$^-$ RBCs. (e) Iron deposit mask from Prussian blue histology. Scale bar 2.5mm. (f) High-iron FeMRI cluster mask. Scale bar 2.5mm. (g) Infiltration mapping using radial rake sampling decile regions overlaid on high-iron MRI cluster mask. Scale bar 2.5mm. 4× expansion shows high-iron FeMRI clusters and decile boundaries. (h) Infiltration profile showing number of histological iron deposits from Prussian blue (PB) and high-iron FeMRI pixel clusters (FeMRI) as a function of percent (%) infiltration into the MMTV-PyMT TS1 mammary tumors. (mean + s.e.m. n=3 tissue cross-sections, n.s. $p>0.05$ Kolmogorov-Smirnov test). **[1 column width]**

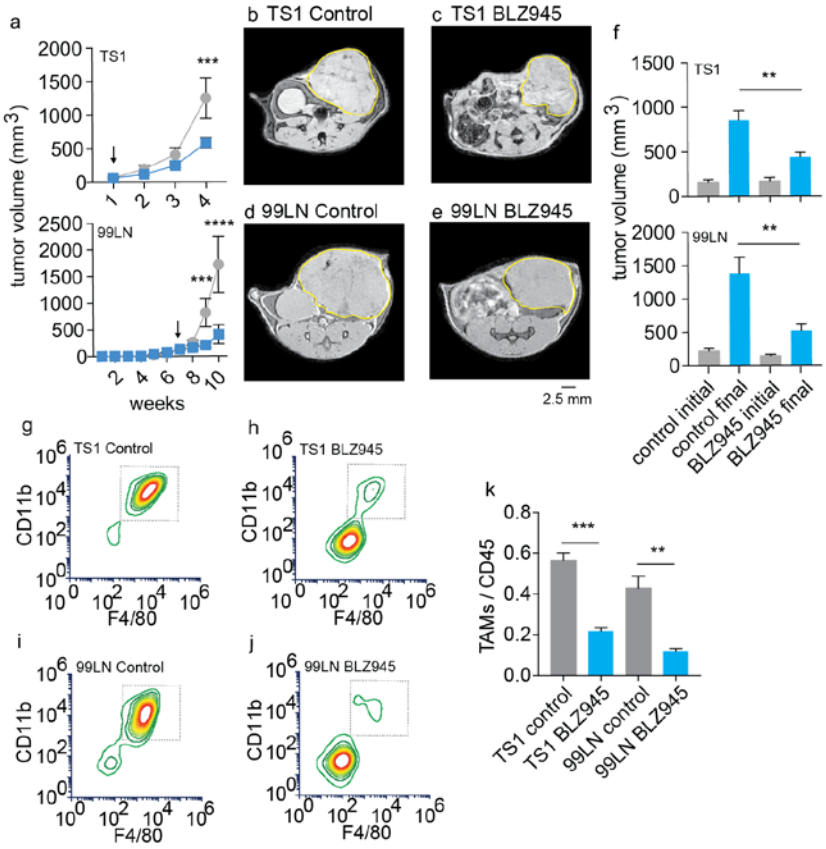

Figure 2. Validation of CSF1R immunotherapy effects on tumor growth and TAM accumulation in PyMT-MMTV breast cancer models. (a) Murine breast tumor models were established by orthotopic mammary fat pad injections and measured by caliper in TS1 and 99LN models during administration of the CSF1R inhibitor BLZ945 (200mg/kg). Arrows indicate start of BLZ945 treatment (mean+s.e.m. n=5 mice/group, ***p<0.001, ****p<0.0001, 2-way ANOVA with Tukey's multiple comparison test). (b) Representative first-echo images from MGE MRI experiments made at study endpoints in control and BLZ945 treated (b-c) TS1 and (d-e) 99LN MMTV-PyMT models. (f) Pre-treatment and endpoint tumor volumes measured by MRI in the CSF1R inhibitor trials. (mean+s.e.m., n=8 mice/group, **p<0.01, two-tailed unpaired students t-test). Flow cytometry panels of TAMs (live $CD45^+Ly6c^-Ly6g^-$ cells gated on $CD11b^+F4/80^+$ cells) obtained from control and BLZ945 treated (g-h) TS1, and (i-j) 99LN tumors. (k) TAM frequency with respect to total $CD45^+$ myeloid cells in the TS1 and 99LN CSF1R inhibitor trials (mean+s.e.m. n=4 mice/group, ** p<0.01, ***P<0.001, two-tailed unpaired students t-test). **[1.5 column width]**

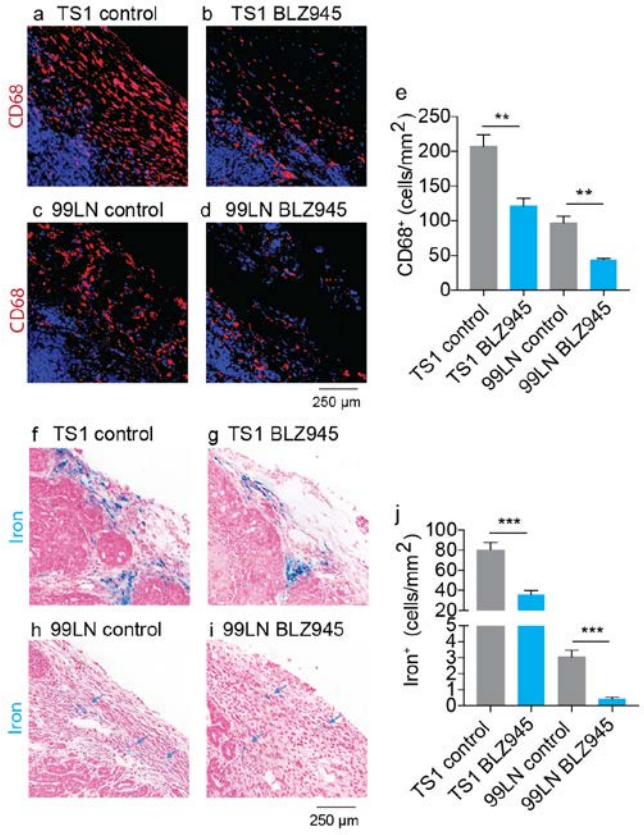

Figure 3. CD68 immunofluorescence and Prussian blue imaging of macrophage iron deposits in MMTV-PyMT murine breast cancer models of CSF1R immunotherapy. Representative CD68 macrophage immunofluoresent imaging in control and BLZ945 treated (a-b) TS1, and (c-d) 99LN tumors. Scale bar 250 µm (e) Absolute counts of $CD68^+$ macrophages per mm^2 MMTV-PyMT tumor cross-section in BLZ945 CSF1R inhibitor trials (mean+s.e.m. n=4 mice/group, **p<0.01, two-tailed unpaired students t-test). Representative iron staining using Prussian blue iron histochemistry in control and BLZ945 treated MMTV-PyMT (f-g) TS1, and (h-i) 99LN tumors. Scale bar 250 µm (j) Absolute counts of $iron^+$ macrophages per mm^2 tumor cross-section in the CSF1R inhibitor trials (mean+s.e.m. n=4 mice/group, ***p<0.001, two-tailed unpaired students t-test). **[1 column width]**

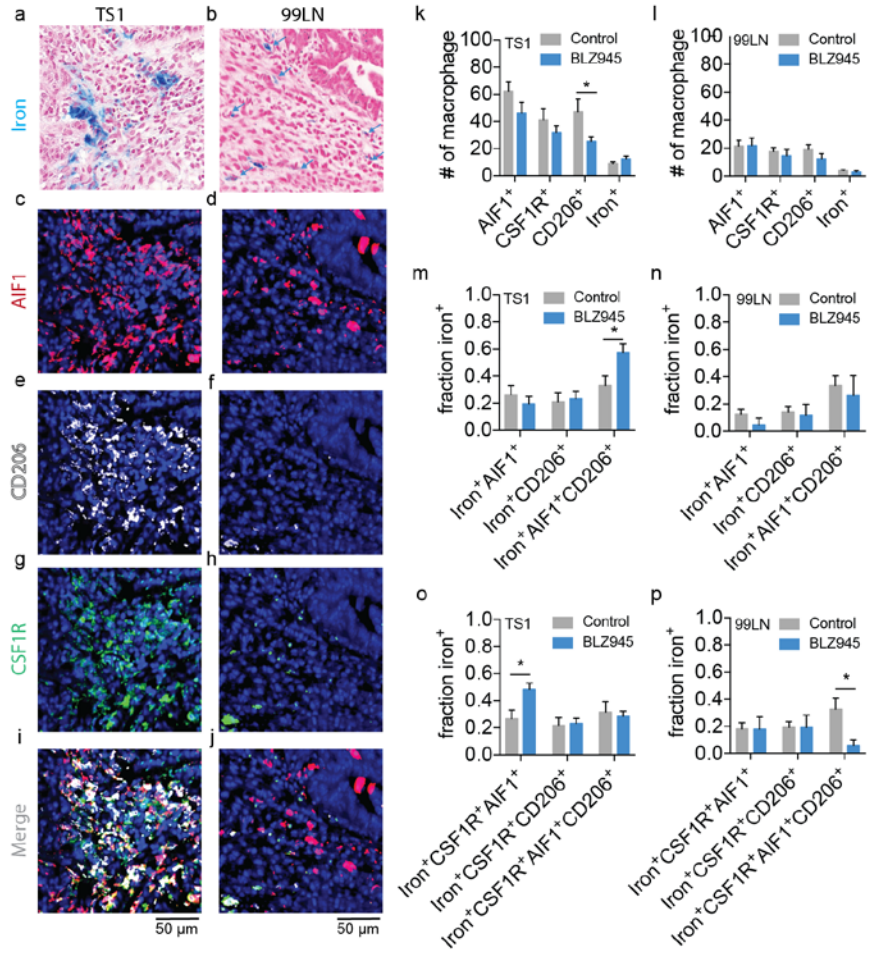

Figure 4. Immunofluorescent and Prussian blue imaging of macrophage iron deposit polarization and CSF1R status in MMTV-PyMT murine breast cancer models of CSF1R immunotherapy. Representative registered fields centered on TAM iron deposits in MMTV-PyMT TS1 and 99LN tumors stained for iron with Prussian blue (a,b), allograft inflammatory factor-1 (AIF1, M1-like, c,d), mannose receptor (CD206, M2-like, e,f), colony stimulating factor 1 receptor (CSF1R, g,h) and the combined immunofluorescent channels(i,j). Note fields of control tumors are shown, but are representative of both control and BLZ945 treated groups. Each field is 200 µm × 200 µm. Scale bar 50 µm. Blue arrows indicate location of iron$^+$ macrophage in 99LN field. Number (#) of AIF1$^+$, CSF1R$^+$, CD206$^+$ and iron$^+$ macrophages detected per field for control and BLZ945 treated (k) TS1 and (l) 99LN MMTV-PyMT mammary tumor models (mean+s.e.m. n=20 fields for TS1 control and BLZ945, n=20 fields for 99LN control and n=7 fields for 99LN BLZ945, *p<0.05, Mann-Whitney test). Fraction of total iron$^+$AIF1$^+$, iron$^+$CD206$^+$, and iron$^+$AIF1$^+$CD206$^+$ macrophages detected per field in control and BLZ945 treated groups for (m) TS1 and (n) 99LN mammary tumor models. Fraction of total iron$^+$CSF1R$^+$AIF1$^+$, iron$^+$CSF1R$^+$CD206$^+$ and iron$^+$CSF1R$^+$AIF1$^+$CD206$^+$ macrophages detected per field in control and BLZ945 treated groups for (o) TS1 and (p) 99LN mammary tumor models (mean+s.e.m. n=20 fields for TS1 control, n=20 fields TS1 BLZ945, n=20 fields for 99LN control and n=7 fields for 99LN BLZ945, *p<0.05, Mann-Whitney test). **[1.5 column width]**

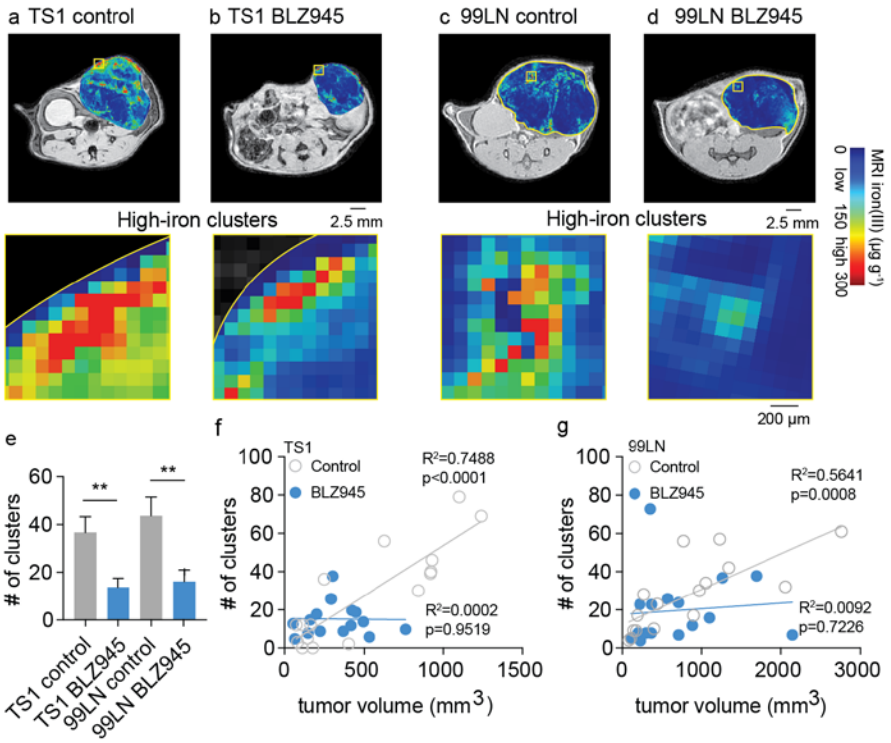

Figure 5. In vivo iron MRI (FeMRI) of murine macrophage iron deposits and correlation between immune and therapeutic CSF1R inhibitor response. Representative in vivo FeMRI axial cross sections of the mammary tumors are shown in control and BLZ945 treated (a-b) TS1, and (c-d) 99LN models. Scale bar 2.5mm. Expansions show high-iron pixel clusters. Scale bar 200 μm. (e) Number (#) of high-iron FeMRI pixel clusters in the TS1 and 99LN tumors in the CSF1R inhibitor trials (mean+s.e.m. n=8 mice/group, **p<0.01 two-tailed unpaired students t-test). Linear correlations between high-iron FeMRI clusters and tumor volumes in the control(○) and BLZ945-treated(●) (f) TS1 and (g) 99LN MMTV-PyMT tumor models (n=8 mice/group, R^2 and correlation p-value from linear Pearson correlation are shown). **[1.5 column width]**

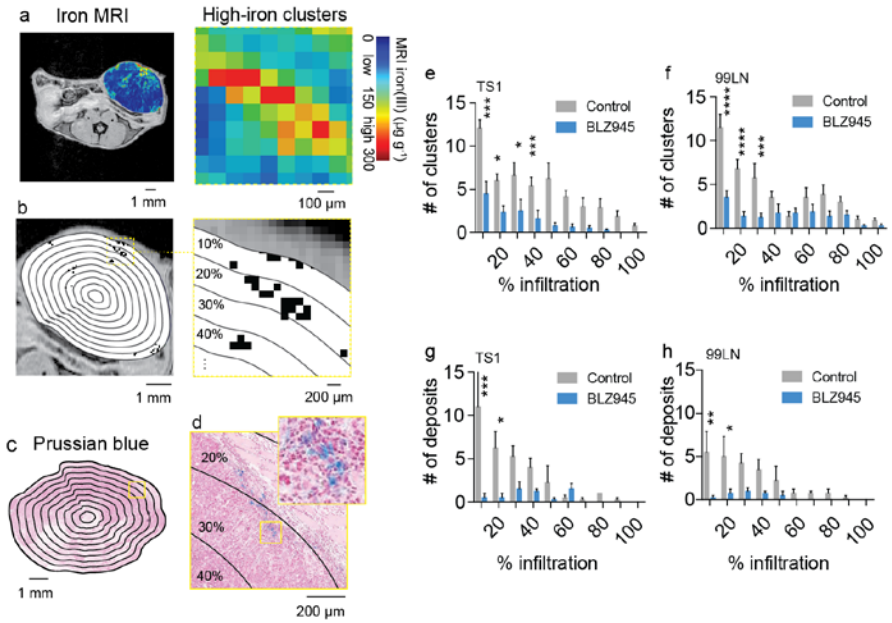

Figure 6. Spatial scores of murine tumor macrophage infiltration in CSF1R immune therapy trials from iron MRI and Prussian blue iron histology. (a) In vivo iron MRI (FeMRI) of MMTV-PyMT mammary tumor. Scale bar 1mm. Expansion shows high-iron pixel clusters. Scale bar 100 μm. (b) Binary high-iron pixel cluster mask from FeMRI of MMTV-PyMT tumor cross-section. Scale bar 1mm. Concentric rake region of interest grid overlay used to profile clusters is shown. Expansion shows detected clusters and concentric counting grid. Scale bar 200 μm. (c) Prussian blue iron stained cross-section of MMTV-PyMT tumor showing the rake grid overlay used to score the iron deposits. Scale bar 1mm. (d) Expansion showing deposit, i.e. colony of $iron^+$ macrophages. Scale bar 200 μm. Infiltration profiles of high-iron clusters from FeMRI in control and BLZ945-treated (e) TS1 and (f) 99LN MMTV-PyMT models (mean+s.e.m. n=8 mice/group, *p<0.05, ***p<0.001, ****p<0.0001, 2-way ANOVA with Sidak's multiple comparison test). $Iron^+$ macrophage deposit infiltration profiles from Prussian blue histology in control and BLZ945-treated (g) TS1 and (h) 99LN MMTV-PyMT models (mean+s.e.m. n=4 mice/group, *p<0.05, ***p<0.001, ****p<0.0001, 2-way ANOVA with Sidak's multiple comparison test). **[1.5 column width]**

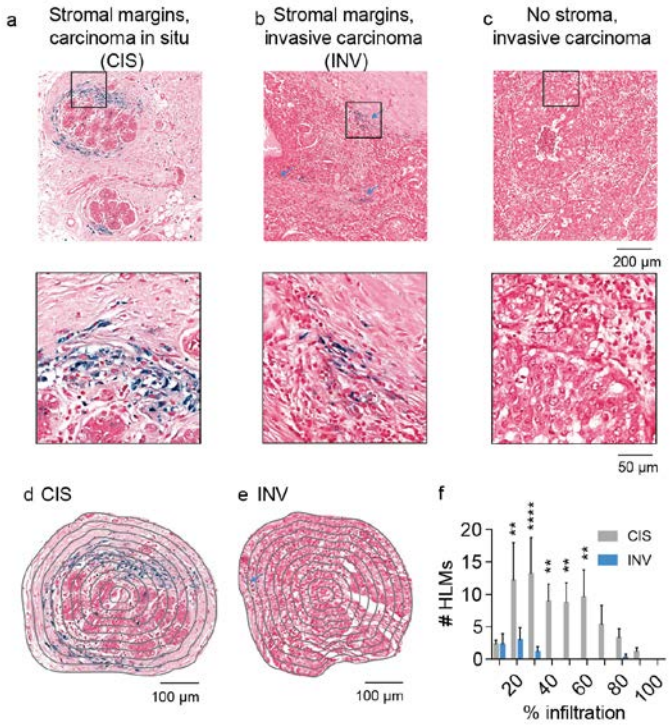

Figure 7. Spatial scores of iron deposits from Prussian blue histology in human breast cancer. Prussian Blue iron histochemistry shows the presence of iron deposits in (a) stromal margins of carcinoma in situ (CIS) and (b) invasive carcinoma (INV, blue arrows). No iron deposits were associated with (c) invasive carcinoma exhibiting poorly defined stromal margins. Scale bar 200µm. Expansions of boxes in (a-c) shown below. Scale bar 40µm. Concentric rake region of interest grid overlay used to profile HLMs in (d) CIS and (e) INV fields. Scale bar 100µm. (f) $Iron^{+}$ macrophage (HLM) infiltration profiles from Prussian blue histology in CIS and INV fields. (mean+s.e.m. n=5 fields/cancer subtype, **p<0.01, ****p<0.0001, 2-way ANOVA with Sidak's multiple comparison test). **[1 column width]**

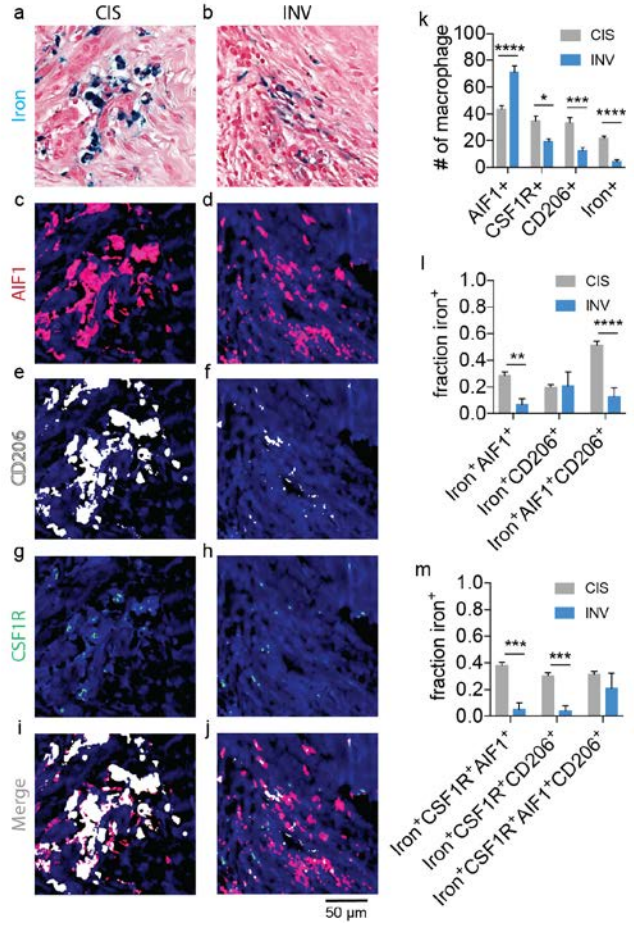

Figure 8. Immunofluorescent and Prussian blue imaging of human macrophage iron deposit polarization and CSF1R status. Representative registered fields of human carcinoma in situ (CIS) and invasive carcinoma where iron deposits are found (INV) stained for iron with Prussian blue (a,b), allograft inflammatory factor-1 (AIF1, c,d), mannose receptor (CD206, e,f), colony stimulating factor 1 receptor (CSF1R, g,h) and the combined immunofluorescent channels (i,j). Each field is 200 µm × 200 µm. Scale bar 50 µm. (k) Number (#) of $AIF1^+$, $CSF1R^+$, $CD206^+$ and $iron^+$ macrophages detected per CIS and INV field. (mean+s.e.m. n=18 fields for CIS, n=9 fields for INV, *p<0.05, ***p<0.001, ****p<0.0001, Mann-Whitney test). (l) Fraction of total $iron^+AIF1^+$, $iron^+CD206^+$, and $iron^+AIF1^+CD206^+$ macrophages detected per CIS and INV field. (m) Fraction of total $iron^+CSF1R^+AIF1^+$, $iron^+CSF1R^+CD206^+$, and $iron^+CSF1R^+AIF1^+CD206^+$ macrophages detected per CIS and INV field (mean+s.e.m. n=18 fields for CIS, n=10 fields for INV, **p<0.01, ***p<0.001, ****p<0.0001, Mann-Whitney test). **[1 column width]**

References

1. Gentles, A.J., et al., *The prognostic landscape of genes and infiltrating immune cells across human cancers.* Nat. Med., 2015. **21**(8): p. 938-945.
2. Leek, R.D., et al., *Association of macrophage infiltration with angiogenesis and prognosis in invasive breast carcinoma.* Cancer Res., 1996. **56**(20): p. 4625-9.
3. Pollard, J.W., *Tumor-educated macrophages promote tumor progression and metastasis.* Nat. Rev. Cancer, 2004. **4**: p. 71-78.
4. Quail, D.F. and J.A. Joyce, *Microenvironmental regulation of tumor progression and metastasis.* Nat Med, 2013. **19**(11): p. 1423-37.
5. Gordon, S., A. Pluddemann, and F.M. Estrada, *Macrophage heterogeneity in tissues: phenotypic diversity and functions.* Immunol. Rev., 2014. **262**: p. 36-55.
6. Van Overmeire, E., et al., *Mechanisms driving macrophage diversity and specialization in distinct tumor microenvironments and parallelisms with other tissues.* Front. Immunol., 2014. **5**: p. 127.
7. Perez-Medina, C., et al., *PET imaging of tumor-associated macrophages with 89Zr-labeled high-density lipoprotein nanoparticles.* J. Nucl. Med., 2015. **56**(8): p. 1272-7.
8. Rashidian, M., et al., *Noninvasive imaging of immune responses.* Proc Natl Acad Sci U S A, 2015. **112**(19): p. 6146-51.
9. Walker-Samuel, S., et al., *In vivo imaging of glucose uptake and metabolism in tumors.* Nat. Med., 2013. **19**: p. 1067-1072.
10. Rodrigues, T.B., et al., *Magnetic resonance imaging of tumor glycolysis using hyperpolarized ^{13}C-labelled glucose.* Nat. Med., 2014. **20**: p. 93-97.
11. Zacharias, N., et al., *Towards real-time metabolic profiling with hyperpolarized succinate.* J. Mol. Imaging. Dyn., 2016. **6**: p. 123.
12. Esmaeili, M., et al., *In vivo ^{31}P magnetic resonance spectroscopic imaging (MRSI) for metabolic profiling of human breast cancer xenografts.* J. Magn. Reson. Imaging, 2015. **41**: p. 601-609.
13. Zakian, K.L., et al., *Identification of prognostic markers in bone sarcomas using proton decoupled phosphorus magnetic resonance spectroscopy.* Cancer Res., 2003. **15**: p. 9042-9047.
14. Chen, H.Y., et al., *Assessing prostate cancer aggressiveness with hyperpolarized dual-gent 3D dynamic imaging of metabolism and perfusion.* Cancer Res., 2017. **15**: p. 3207-3216.
15. Longo, D.L., et al., *In vivo imaging of tumor metabolism and acidosis by combining PET and MRI-CEST pH imaging.* Cancer Res., 2016. **15**: p. 6463-6470.
16. Do, Q.N., et al., *Redox - and hypoxia-responsive MRI contrast agents.* ChemMedChem, 2014. **9**: p. 1116-1129.
17. Andrejeva, G. and J.C. Rathmell, *Similarities and distinctions of cancer and immune metabolism in inflammation and tumors.* Cell Metab., 2017. **26**: p. 49-70.
18. Hentze, M.W., M.U. Muckenthaler, and N.C. Andrews, *Balancing acts: molecular control of mammalian iron metabolism.* Cell, 2004. **117**: p. 285-297.
19. Gammella, E., et al., *Macrophages: central regulators of iron balance.* Metallomics, 2014. **6**: p. 1336-1345.

20. Nairz, M., et al., *'Ride on the ferrous wheel' — The cycle of iron in macrophages in health and disease.* Immunobiol., 2015. **220**: p. 280-294.
21. Bovell, E., et al., *Dietary iron-loaded rat liver haemosiderin and ferritin: in situ measurement of iron core nanoparticle size and cluster structure using anomalous small-angle X-ray scattering.* Phys. Med. Biol., 2009. **54**: p. 1209-1221.
22. Leftin, A., et al., *Iron imaging reveals tumor and metastasis macrophage hemosiderin deposits in breast cancer.* PLoS One, 2017. **12**(9): p. e0184765.
23. Leftin, A., et al., *Iron deposition is associated with differential macrophage infiltration and therapeutic response to iron chelation in prostate cancer.* Sci. Rep., 2017. **7**(1): p. 11632.
24. Brooks, R.A., et al., *Comparison of T2 relaxation in blood, brain, and ferritin.* J. Magn. Reson. Imaging, 1995. **5**(4): p. 446-50.
25. Carneiro, A.A., et al., *In vivo tissue characterization using magnetic techniques.* Neurol. Clin. Neurophysiol., 2004. **2004**: p. 85.
26. Fischer, R. and P.R. Harmatz, *Non-invasive assessment of tissue iron overload.* Hematology, 2009. **2009 No. 1**: p. 215-221.
27. Garbowski, M.W., et al., *Biopsy-based calibration of $T2^*$ magnetic resonance for estimation of liver iron concentration and comparison with R2 Ferriscan.* J. Cardiov. Magn. Reson., 2014. **16**.
28. McAuley, G., et al., *Quantification of punctate iron sources using magnetic resonance phase.* Magn. Reson. Med., 2010. **63**(1): p. 106-15.
29. Schenk, J.F., *The role of magnetic susceptibility in magnetic resonance imaging: MRI magnetic compatibility of the first and second kinds.* Med. Phys., 1996. **23**: p. 815-850.
30. Takada, S., et al., *Hemosiderin detected by T2*-weighted magnetic resonance imaging in patients with unruptured cerebral aneurysms: indication of previous bleeding?* Neurol. Med. Chir. (Tokyo), 2011. **51**(4): p. 275-81.
31. Zhou, X., et al., *Three-dimensional NMR microscopy of rat spleen and liver.* Magn. Reson. Med., 1993. **30**(1): p. 92-7.
32. Shapiro, E.M., et al., *MRI detection of single particles for cellular imaging.* Proc. Natl. Acad. Sci. USA, 2004. **101**: p. 10901-10906.
33. Daldrup-Link, H.E., et al., *Imaging of tumor associated macrophages with clinically-applicable iron oxide nanoparticles.* Clin. Cancer Res., 2011. **17**: p. 5695-5704.
34. Weissleder, R., M. Nahrendorf, and M.J. Pittet, *Imaging macrophages with nanoparticles.* Nat. Mater., 2014. **13**: p. 125-138.
35. Maeda, H., *Toward a full understanding of the EPR effect in primary and metastatic tumors as well as issues related to its heterogeneity.* Adv. Drug. Deliv. Rev., 2015. **30**: p. 3-6.
36. Costa da Silva, M., et al., *Iron induces anti-tumor activity in tumor-associated macrophages.* Front. Immunol., 2017. **8**: p. 1479.
37. Laskar, A., et al., *SPION primes THP1 derived M2 macrophages towards M1-like macrophages.* Biochem. Biophys. Res. Commun., 2013. **441**(4): p. 737-42.
38. Zanganeh, S., et al., *Iron oxide nanoparticles inhibit tumour growth by inducing pro-inflammatory macrophage polarization in tumour tissues.* Nat. Nanotechnol., 2016. **11**(11): p. 986-994.

39. Berdoukas, V., T.D. Coates, and Z.I. Cabantchik, *Iron and oxidative stress in cardiomyopathy in thalassemia.* Free Radic. Biol. Med., 2015. **88**: p. 3-9.
40. Fleming, R.E. and P. Ponka, *Iron overload in human disease.* N. Engl. J. Med., 2012. **366**: p. 348-359.
41. Haacke, E.M., et al., *Imaging iron stores in the brain using magnetic resonance imaging.* Magn. Reson. Imaging, 2005. **23**(1): p. 1-25.
42. Wood, J.C., et al., *Liver MRI is more preceise than liver biopsy for assessing total body iron balance: a comparison of MRI relaxometry with simulated liver biopsy results.* Magn. Reson. Imaging, 2015. **33**: p. 761-767.
43. Olson, O.C., et al., *Tumor-associated macrophages suppress the cytotoxic activity of antimitotic agents.* Cell Rep., 2017. **19**(1): p. 101-113.
44. Quail, D.F., et al., *Obesity alters the lung myeloid cell landscape to enhance breast cancer metastasis through IL5 and GM-CSF.* Nat. Cell Biol., 2017. **19**(8): p. 974-987.
45. Shree, T., et al., *Macrophages and cathepsin proteases blunt chemotherapeutic response in breast cancer.* Genes Dev., 2011. **25**(23): p. 2465-79.
46. Strachan, D.C., et al., *CSF1R inhibition delays cervical and mammary tumor growth in murine models by attenuating the turnover of tumor-associated macrophages and enhancing infiltration by CD8(+) T cells.* Oncoimmunology, 2013. **2**(12): p. e26968.
47. Lin, E.Y., et al., *Progression to malignancy in the polyoma middle T oncoprotein mouse breast cancer model provides a reliable model for human disease.* Am. J. Pathol. , 2003. **163**: p. 2113-2126.
48. Lin, E.Y., et al., *Colony-stimulating factor 1 promotes progression of mammary tumors to malignancy.* J. Exp. Med., 2001. **193**(6): p. 727-40.
49. Patel, S. and M.R. Player, *Colony-stimulating factor-1 receptor inhibitors for the treatment of cancer and inflammatory disease.* Curr. Top. Med. Chem., 2009. **9**(7): p. 599-610.
50. Pyontek, S.M., et al., *CSF-1R inhibition alters macrophage polarization and blocks glioma progression.* Nat. Med., 2013. **19**: p. 1264-1276.
51. Zhu, Y., et al., *CSF1/CSF1R blockade reprograms tumor-infiltrating macrophages and improves response to T-cell checkpoint immunotherapy in pancreatic cancer models.* Cancer Res, 2014. **74**(18): p. 5057-69.
52. Ryder, M., et al., *Genetic and pharmacological targeting of CSF-1/CSF-1R inhibits tumor-associated macrophages and impairs BRAF-induced thyroid cancer progression.* PLoS One, 2013. **8**(1): p. e54302.
53. Pyonteck, S.M., et al., *Deficiency of the macrophage growth factor CSF-1 disrupts pancreatic neuroendocrine tumor development.* Oncogene, 2012. **31**(11): p. 1459-67.
54. Yarilin, D., et al., *Machine-based method for multiplex in situ molecular characterization of tissues by immunofluorescence detection.* Sci. Rep., 2015. **5**: p. 9534.
55. Daldrup-Link, H. and L.M. Coussens, *MR imaging of tumor-associated macrophages.* Oncoimmunology, 2012. **1**(4): p. 507-509.
56. Narunsky, L., et al., *Imaging aspects of the tumor stroma with therapeutic implications.* Pharmacol. Ther., 2014. **141**(2): p. 192-208.

57. Ward, R.J., et al., *The role of iron in brain ageing and neurodegenerative disorders.* Lancet Neurol., 2014. **13**: p. 1045-160.
58. Gammella, E., et al., *Macrophages: central regulators of iron balance.* Metallomics, 2014. **6**(8): p. 1336-45.
59. Le, N.T. and D.R. Richardson, *The role of iron in cell cycle progression and the proliferation of neoplastic cells.* Biochim. Biophys. Acta, 2002. **1603**(1): p. 31-46.
60. Marques, O., et al., *Iron homeostasis in breast cancer.* Cancer Letters, 2014. **347**: p. 1-14.
61. Mertens, C., et al., *Intracellular Iron Chelation Modulates the Macrophage Iron Phenotype with Consequences on Tumor Progression.* PLoS One, 2016. **11**(11): p. e0166164.
62. Thulborn, K.R., et al., *The role of ferritin and hemosiderin in the MR appearance of cerebral hemorrhage: a histopathologic biochemical study in rats.* AJR Am. J. Roentgenol., 1990. **154**(5): p. 1053-9.
63. Schindelin, J., et al., *Fiji: an open-source platform for biological-image analysis.* Nat. Methods, 2012. **28**: p. 676-682.

Hindawi
Contrast Media & Molecular Imaging
Article ID 3526438

Research Article

Quantification of Nanoparticle Enhancement in Polarized Breast Tumor Macrophage Deposits by Spatial Analysis of MRI and Histological Iron Contrast Using Computer Vision

Avigdor Leftin[1] **and Jason A. Koutcher**[1,2,3]

[1]*Department of Medical Physics, Memorial Sloan Kettering Cancer Center, New York, NY, USA*
[2]*Department of Medicine, Memorial Sloan Kettering Cancer Center, New York, NY, USA*
[3]*Molecular Pharmacology Program, Memorial Sloan Kettering Cancer Center, New York, NY, USA*

Correspondence should be addressed to Avigdor Leftin; leftina@mskcc.org

Received 7 June 2018; Accepted 13 August 2018

Academic Editor: Filippo Galli

Magnetic resonance imaging applications utilizing nanoparticle agents for polarized macrophage detection are conventionally analyzed according to iron-dependent parameters averaged over large regions of interest (ROI). However, contributions from macrophage iron deposits are usually obscured in these analyses due to their lower spatial frequency and smaller population size compared with the bulk of the tumor tissue. We hypothesized that, by addressing MRI and histological pixel contrast heterogeneity using computer vision image analysis approaches rather than statistical ROI distribution averages, we could enhance our ability to characterize deposits of polarized tumor-associated macrophages (TAMs). We tested this approach using *in vivo* iron MRI (FeMRI) and histological detection of macrophage iron in control and ultrasmall superparamagnetic iron oxide (USPIO) enhanced mouse models of breast cancer. Automated spatial profiling of the number and size of iron-containing macrophage deposits according to localized high-iron FeMRI or Prussian blue pixel clustering performed better than using distribution averages to evaluate the effects of contrast agent injections. This analysis was extended to characterize subpixel contributions to the localized FeMRI measurements with histology that confirmed the association of endogenous and nanoparticle-enhanced iron deposits with macrophages in vascular regions and further allowed us to define the polarization status of the macrophage iron deposits detected by MRI. These imaging studies demonstrate that characterization of TAMs in breast cancer models can be improved by focusing on spatial distributions of iron deposits rather than ROI averages and indicate that nanoparticle uptake is dependent on the polarization status of the macrophage populations. These findings have broad implications for nanoparticle-enhanced biomedical imaging especially in cancer.

1. Introduction

Widespread efforts have succeeded in integrating nanoparticles in virtually all areas of medical imaging. The appeal of these formulations derives from their ability to be tailored to specific applications ranging from neuroscience to oncology by chemical manipulation of nanoparticle composition rendering them visible to multiple imaging modalities such as MRI, PET, and optical imaging systems [1]. Moreover, the ability to functionalize these particles using delivery systems such as polymers or lipids and bioaffinity tags such as antibodies further enhances our ability to probe, monitor, and control ubiquitous biological processes spanning drug delivery and cell tracking [2].

Nanoparticles formulated from iron are ubiquitous contrast agents for MRI. One common agent used consists of ultrasmall superparamagnetic iron oxide (USPIO) nanoparticles solubilized with dextran polymer to facilitate suspension and delivery in aqueous solution [3, 4]. Cancer research is a premier application of these USPIO nanoparticles, and they have been used to investigate virtually every cancer type. They provide information about both vascular and immune cell properties of the tumor that are key determinants of the pharmacodynamic behavior of

drugs and the cellular immune response to therapies [5–7].

Quantification of tissue uptake of iron nanoparticles and deposition in macrophages is conventionally performed using region of interest (ROI) analysis of MRI images [8]. Pixel contrast levels, relaxation times, rates, or the susceptibility phase [9–12] are measured over tissue cross-sectional areas and analyzed according to pixel distribution statistics. Changes in iron concentration following USPIO injection can be further quantified from these pixel distributions according to parametric relations between these observables and known iron standards, iron-labeled cells, or biopsy iron measurement to provide quantitative estimates on nanoparticle delivery, cellular uptake, and concentration [13–16]. So-called iron MRI (FeMRI) approaches can estimate iron nanoparticle uptake by the measurement of parametric distribution statistics. However, it has long been an accepted caveat of the quantitative interpretation of most cellular MRI applications that ROI-based distribution analysis is biased by contributions from the abundant low-iron areas of the tissue, i.e., those not containing the iron deposit or contrast agent, which limits the specificity of the MRI pixel distribution analysis for iron accumulation in rare cellular targets such as macrophages in tumors.

Macrophages are important imaging targets in cancer because they can function in both inflammatory and wound-healing roles that influence tumor growth and therapeutic response [17–19]. Nanoparticle injection and uptake is dependent upon and can influence this polarization status of the targeted cellular populations as these cells exhibit plasticity in these functional roles that in turn is coupled to their innate role in iron metabolism [20, 21]. While MRI studies do not directly report on polarization, immunofluorescence imaging can be used to evaluate changes in TAM iron deposit polarization and provide subpixel information about the dependence of the USPIO contrast agent uptake on TAM polarization [22–24]. However, nanoparticle delivery to the tumor rarely exceeds a few percent of the injected dose [25], and therefore, only a small fraction of macrophages present in the tumor will be engaged by the nanoparticles and give rise to localized detectable iron contrast. Therefore, similar to cellular iron MRI, whole ROI analysis of histological polarization state measurements is more representative of the nanoparticle-free macrophage populations rather than subpopulations containing iron. Therefore, scoring macrophage polarization with immunofluorescence using whole ROI distribution analysis also will generally not be representative of the relatively rare iron-handling populations targeted by the nanoparticle injections. Thus, alternative unbiased analysis approaches that better quantify the local distributions of these iron-containing cells and their phenotypes are required to evaluate the polarization status of the macrophage targets and to provide cellular level corroboration of FeMRI applications.

In the current study, we advance a computer vision approach to localize polarized macrophages according to iron status in order to improve their quantification in USPIO-enhanced cellular imaging by MRI and histology. We have previously shown that, by addressing the spatial heterogeneity of iron-dependent image contrast, we could enhance the quantification of these macrophage deposits without contrast agents using MRI and histology because the type of iron stored in the macrophages generates stronger MRI contrast enhancement compared with venous or hemorrhagic blood [26–30] and Prussian blue only labels macrophage with solid iron deposits corresponding to those of the highest iron concentration. These endogenous stores conferred sufficient cellular sensitivity and specificity to detect macrophage iron deposits in multiple cancer models including prostate cancer and breast cancer, in both primary and distant disseminated metastatic locations of the lung and brain, as well as systemically in organs which naturally or pathologically accumulate macrophage iron such as the liver and spleen [29, 30]. In the current study, we continue our translational development of this approach by combining it with the USPIO contrast agent injection to evaluate iron deposition in polarized breast tumor macrophages.

2. Results

To demonstrate the difference between the ROI average distribution measurements and the localized measurements of cellular iron deposition with and without dextran-USPIO injection, we initiated orthotopic MMTV-PyMT murine mammary tumors and injected USPIO (0.5 mmol/kg) or saline intravenously once tumor volumes reached approximately 1 cm^3. Mapping iron-dependent contrast 24 hrs after injection at 7T showed that both the nanoparticle-free (Figure 1(a), −USPIO) and contrast-enhanced tumors (Figure 1(b), +USPIO) evidenced heterogeneous distributions of pixel iron levels, with both cohorts exhibiting numerous high-iron pixel regions, i.e., clusters indicative of iron deposits, at the periphery of the tumor, and iron oxide-injections increased the numbers of these clusters.

Analysis of the iron MRI maps was then performed to quantify these pixel distributions. Parametric pixel distributions expressed as number of pixel clusters (Figure 1(c)) and cluster size measured in mm^2 (Figure 1(d)) were reconstructed as a function of iron concentration with high and low ranges defined with respect to the median iron level of the distribution range. Frequency (number of pixel clusters) and size distribution maxima fell well within the low-iron contrast range in both control and USPIO-injected tumors and appeared to shift nominally towards higher concentrations with USPIO injection. In the high iron range of the frequency distribution, clear increases of pixel clusters occurred with the USPIO uptake, while the size of these high-iron clusters appeared to remain constant in the control and nanoparticle-treated groups suggesting that iron injection changed only the number of the deposits but not their size. Statistical analysis of the ROI-based parametric iron distributions was then performed to quantify the observations. First, median values were calculated from ROI analysis over whole tumor cross sections as is conventionally performed. Median iron levels of the parametric pixel distributions from the ROI showed small but significant increases in frequency (Figure 1(e); $p < 0.05$) and size (Figure 1(f); $p < 0.05$) with USPIO enhancement. In

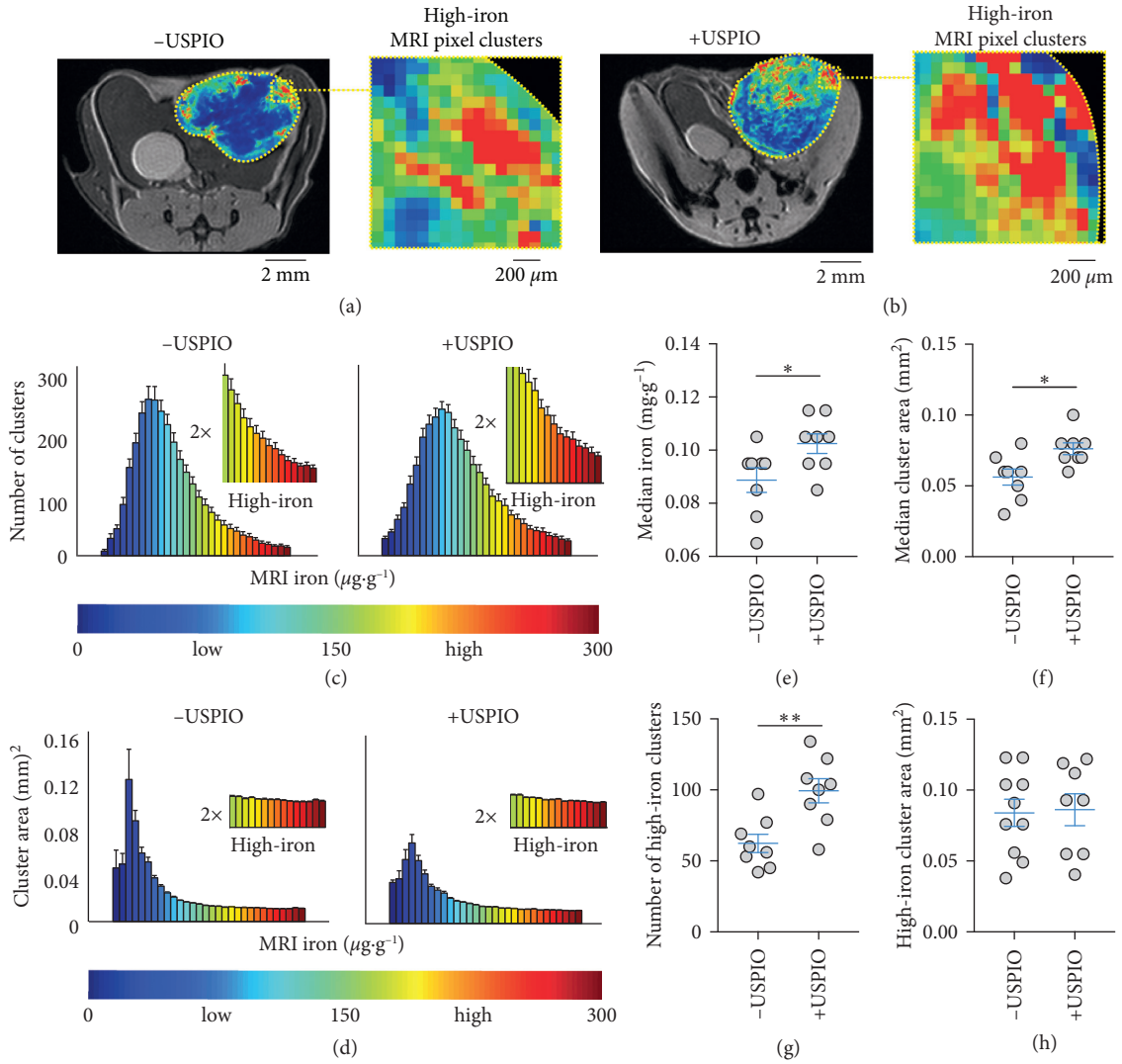

FIGURE 1: Spatial quantification of endogenous and nanoparticle-enhanced iron deposits with MRI *in vivo*. T_2-weighted MRI and iron concentration overlay images of (a) control (–USPIO) and (b) iron nanoparticle-injected (+USPIO) tumors. Expansion shows high-iron pixel contrast in clustered areas. (c) Number (#) of clusters and (d) area of the pixel clusters in control (–USPIO) and nanoparticle-injected (+USPIO) tumors as a function of iron concentration. Distributions are from whole cross-sectional regions of interest (ROI) areas of tumors measuring approximately 1 cm^3 (mean ± SEM shown, $n = 8$ tumors/group). MRI iron concentration range at bottom corresponds to values in iron images above. Control (–USPIO) and nanoparticle-injected (+USPIO) (e) median iron concentrations and (f) pixel cluster sizes. (g) Number (#) of high-iron pixel clusters and (h) size of the high-iron clusters from localized computer vision analysis (mean ± SEM shown, $n = 8$ tumors/group, n.s. $p > 0.05$, $^{*}p < 0.05$, $^{***}p < 0.001$, two-tailed unpaired Student's t-test). Scale bars are shown for all images.

order to more specifically quantify local accumulation of iron deposits indicated by the high-iron range stratification, the frequency of high-iron clusters in the maps was counted, and the areas were measured. This revealed significant increases of the high-iron pixel clusters with iron nanoparticle injection (Figure 1(g); $p < 0.001$) and provided an additional measurement of the size of these regions of iron accumulation with and without contrast agents (Figure 1(h); $p > 0.05$). This demonstrates an improvement over the ROI quantification in terms of the significant increases in iron deposit accumulation detected and confirms the observation that the number of high-iron clusters increase but the size remains relatively unchanged with USPIO injection.

To confirm the cellular identity of the iron$^+$ species and characterize the microenvironment of the iron deposits, Prussian blue iron histochemistry (Figure 2(a)) and immunofluorescence for F4/80$^+$ (Figure 2(b)) macrophages and CD31$^+$ vasculature (Figure 2(c)) was performed. Iron staining of the MMTV-PyMT tumor sections evidenced iron$^+$ cellular species in stromal regions almost exclusively at peripheral tumor margins. These localized cellular iron sources clustered as multicellular deposits in both the control and USPIO-treated tumors. Macrophage immunofluorescence of these tissue cross sections further confirmed that the iron$^+$ cells identified in the Prussian blue histology were colocalized with F4/80$^+$ macrophages. These iron$^+$ F4/80$^+$ macrophages were

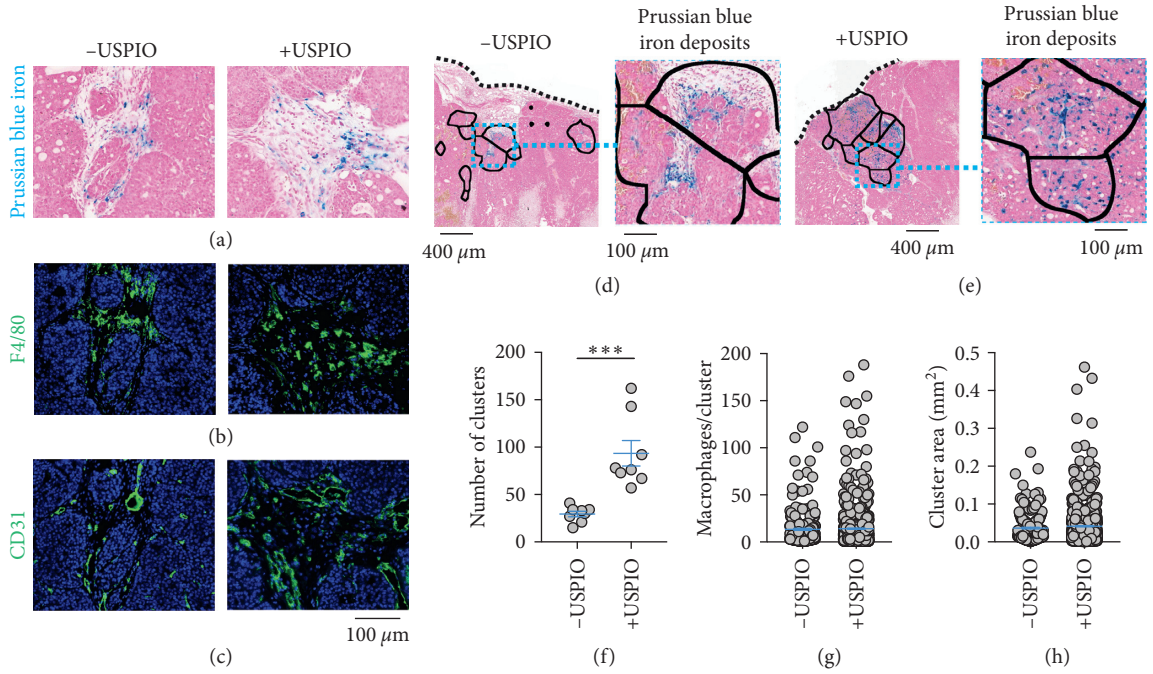

FIGURE 2: Spatial quantification of endogenous and contrast-enhanced macrophage deposits by iron histology. Paraffin-embedded sections from control (−USPIO) and iron nanoparticle-injected (+USPIO) tumors. (a) Prussian blue iron staining, (b) F4/80 macrophage immunofluorescence, and (c) CD31 vascular immunofluorescence were performed in the same sections to demonstrate the colocalization of iron deposits with infiltrating macrophages in vascular areas of the tumor microenvironment. Histological fields from (d) control and (e) iron nanoparticle-injected mice showing deposits of Prussian blue iron$^+$ macrophages localized in infiltrative border regions in discrete clusters. Black borders are regions of interest drawn automatically around deposits of cells according to iron status. Expansion shows iron$^+$ macrophages in the deposit regions. (f) Number of iron deposits (clusters) per tumor cross section in control (−USPIO) and nanoparticle-injected (+USPIO) mice (mean ± SEM shown, $n = 8$ tumors/group, $^{***}p < 0.001$, two-tailed unpaired Student's t-test). (g) Number of iron$^+$ macrophages per deposit, and (h) size of each of the deposits measured over the whole Paraffin-embedded tumor cross sections stained by Prussian blue (mean ± SEM shown, −USPIO $n = 235$ total clusters/group, +USPIO $n = 748$ total clusters/group, n.s. $p > 0.05$). Scale bar is shown for all images.

invariably found in close proximity to CD31$^+$ vasculature in both control and USPIO-injected cohorts suggesting that the accumulation of metabolic or nanoparticle-derived iron is dependent upon their spatial distribution beside tumor vasculature.

The spatial characteristics of the histologically detected macrophage iron deposits were then analyzed in a manner similar to the FeMRI pixel cluster analysis. The endogenous (Figure 2(d)) and USPIO-enhanced deposits (Figure 2(e)) found in the localized regions were automatically identified and the number of the clusters (Figure 2(f)), the number of iron$^+$ macrophages per deposit (Figure 2(g)), and the areas of the clusters (Figure 2(h)) were measured exhaustively from whole tumor axial cross sections. The number of deposits containing iron$^+$ macrophages increased significantly with USPIO injection ($p < 0.001$), and deposit areas in the control and injected groups were found to be equivalent, approximately a few MRI square-pixels ($p > 0.05$). These regions also equivalently contained an average of approximately 14 iron$^+$ macrophages per control or USPIO-enhanced deposit ($p > 0.05$) supporting the cellular sensitivity of the FeMRI measurement and specificity of the pixel cluster analysis for these cellular species.

To determine the polarization status of general macrophage populations in the tumors and their changes with injection of USPIO, immunofluorescence staining of the tumor cross sections was conducted for pan-macrophage (CD68), inflammatory (M1-like AIF1 (allograft inflammatory factor 1)), and wound-healing surface marker phenotypes (M2-like CD206 (mannose receptor)), besides Prussian blue iron histology as the primary observable (Figures 3(a)–3(e)). Absolute counts of CD68$^+$ macrophages conducted over whole tissue cross-sectional areas were performed to score CD68 infiltrates (Figure 3(f); $p > 0.05$). AIF1$^+$ and CD206$^+$ polarization markers were similarly quantified to evaluate phenotypic shifts. Exhaustive counts performed over the control tumor cross sections and calculation of frequency of these populations with respect to total numbers of these macrophages (M1 or M2/(M1+M2)) (Figure 3(g)) showed that USPIO injection did not lead to significant changes in absolute counts of macrophages ($p > 0.05$). Phenotypic populations in the control mice were significantly biased towards M2-like polarization with 42% M1-like AIF1$^+$ and 58% of macrophages CD206$^+$ ($p < 0.05$). This analysis of TAM

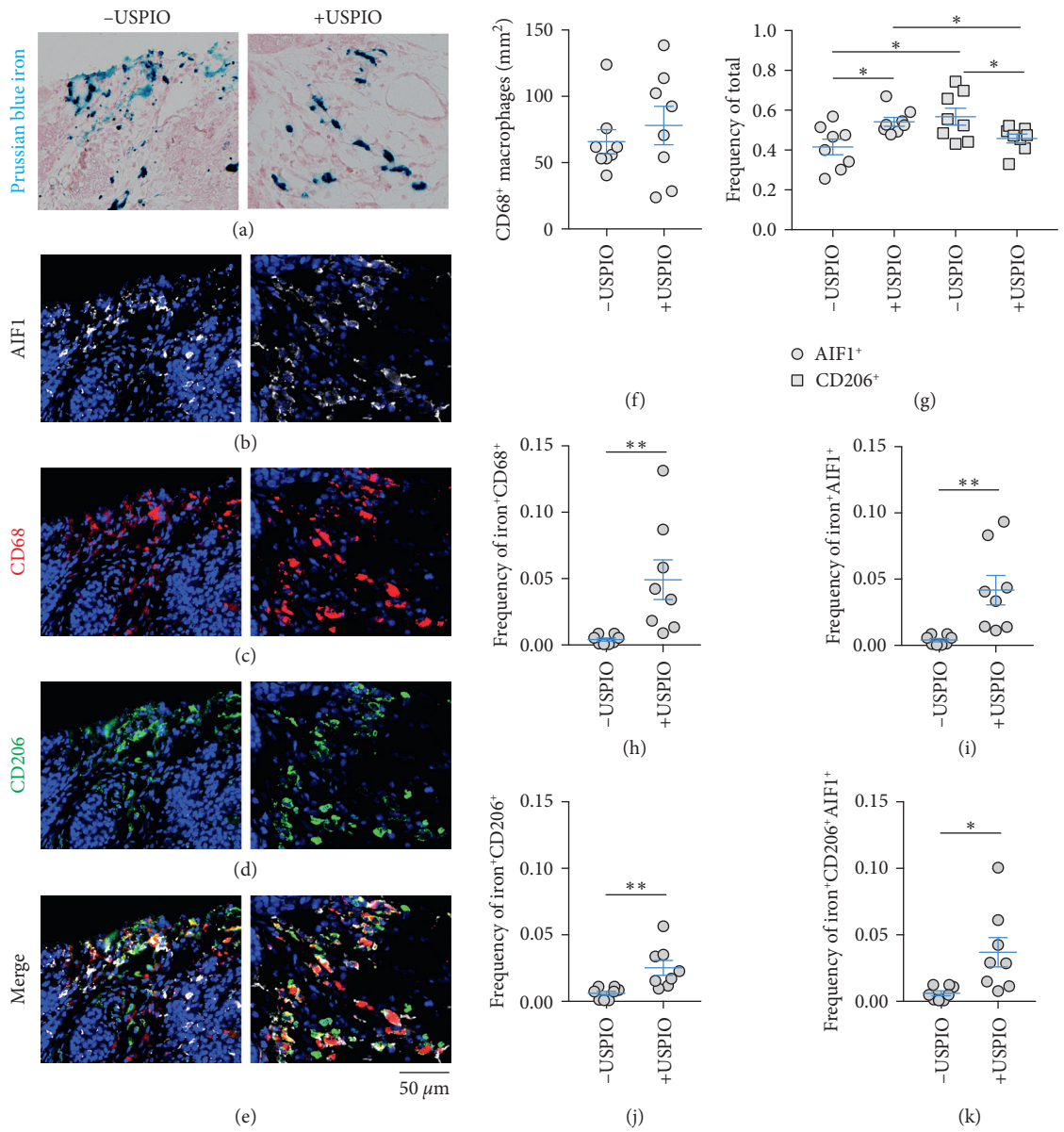

Figure 3: Characterization of endogenous and contrast-enhanced macrophage iron deposit polarization. Fields of paraffin-embedded tumor cross sections from control (left, –USPIO) and iron nanoparticle-injected (right, +USPIO) mice showing deposits of (a) Prussian blue iron$^+$ macrophages and colocalized (b) AIF1, (c) CD68, (d) CD206, and (e) merged immunofluorescent markers. (f) Absolute count of CD68$^+$ macrophages per mm^2 tumor cross section and (g) frequency of total M1-like (AIF1) and M2-like (CD206) macrophages determined by whole tumor cross section ROI analysis of immunofluorescent images in control (–USPIO) and nanoparticle-injected (+USPIO) cohorts (mean ± SEM shown, $n = 8$ tumors/group, $^*p < 0.05$, two-tailed Student's t-test). Frequency of total iron$^+$ macrophage calculated as (h) iron$^+$CD68$^+$/CD68$^+$, (i) iron$^+$AIF1$^+$/AIF1$^+$, (j) iron$^+$CD206$^+$/CD206$^+$, and (k) iron$^+$CD206$^+$AIF1$^+$/CD206$^+$AIF1$^+$ cells (mean ± SEM shown, $n = 8$ tumors/group, $^*p < 0.05$, $^{**}p < 0.01$, two-tailed Student's t-test). Scale bar is shown for all images.

polarization was also performed in the USPIO-injected animals and showed that M1 and M2 status was significantly different with 54% AIF1$^+$ and 46% CD206$^+$ TAMs present ($p < 0.05$) indicating that USPIO injection caused a significant increase in M1-like cells and reduction of M2-like cells ($p < 0.05$). This demonstrates that TAM polarization and not number of macrophages in the tissue changed as a function of iron nanoparticle injection in these measurements.

We then measured the frequency of specifically iron$^+$-polarized TAMs with respect to their respective general population (iron$^+$M1$^+$ or iron$^+$M2$^+$/M1$^+$ or M2$^+$), performed counts of iron$^+$CD68$^+$ cells as a function of total CD68, and also counted the frequency of the iron$^+$AIF1$^+$CD206$^+$ population expressing both general macrophage polarization markers selected in this study (Figures 3(h)–3(k)). The numbers of iron$^+$ cells were less frequent than the general populations assessed above. In control tumors, 0.41% were

iron$^+$, 0.40% of AIF1$^+$ were iron$^+$, 0.61% of CD206$^+$ TAMs were iron$^+$, and 0.60% were iron$^+$AIF1$^+$CD206$^+$ cells. Injection of USPIO led to significant increases in all these macrophage subsets with 4.9% iron$^+$CD68$^+$ cells ($p < 0.01$), 4.1% iron$^+$AIF1$^+$ ($p < 0.01$), 2.5% iron$^+$CD206$^+$ ($p < 0.01$), and 3.7% iron$^+$AIF1$^+$CD206$^+$ cells observed after USPIO injection ($p < 0.05$). This indicates that SPIO injection increases iron in all polarized macrophage subsets but also indicates that inflammatory subsets take up relatively, but not significantly ($p > 0.05$), more iron than M2-like populations.

3. Discussion

The main purpose of the current work was to evaluate a computer vision method for detection and quantification of USPIO-enhanced macrophages by MRI and extend this analysis to histological images in order to characterize sub-MRI pixel phenotypes of the cells. By targeting the spatial heterogeneity in iron-based pixel contrast arising from endogenous or iron contrast agent-enhanced cellular iron deposits, this approach improved statistical quantification of macrophages over conventional ROI-average distribution analysis, and provided measured constraints on the size and frequency of the polarized macrophage deposits.

The MRI analysis approach presented here improves on current conventional ROI-based approaches by parsing the spatial distributions of iron image contrast. This was accomplished by constructing parametric iron MRI maps and then quantifying the number and size of pixel cluster areas as a function of stratified iron concentration range. This indicated that most of the area of tumor pixels in both control and nanoparticle-injected groups were predominantly of low iron contrast, reflecting a cellular distribution characteristic of the location of low-iron cancer cells and stroma in the tumor. The ROI distribution analysis only revealed minor shifts towards high iron concentrations with USPIO injection, while counting of the localized iron clusters increased the statistical differences between the control and USPIO-injected groups. A similar approach was used to evaluate the size of macrophage iron deposits in the histological analysis with and without contrast agents. This revealed areas of iron-laden macrophage colonies that were on the order of the size and frequency of the high-iron MRI clusters. This side-by-side spatial analysis confirmed the cellular sensitivity and specificity of the MRI and histological methods for detecting localized macrophage deposits according to the iron status, and provided per unit area cellularity estimates of the iron-laden macrophages detected in vivo by MRI.

To complement the iron histology analysis, we also performed immunofluorescent imaging focusing on the microenvironment and polarization characteristics of both general macrophage populations and specifically the iron$^+$ macrophage subpopulations. The polarization of macrophages is a multifactorial process that depends on the tissue and microenvironment in which they are found as well as complex signaling between tissue resident and infiltrating immune cells with the macrophages [31, 32]. As such, myriad intracellular and surface protein markers have been developed that allow one to specify their position along the continuum of accessible polarization states [33]. Iron itself is a central metabolic factor in macrophage function and is associated with many polarization states [21]. To determine the association of iron deposits with the tumor microenvironment and polarization, we adopted a panel of general tissue and macrophage biomarkers which showed the iron$^+$ macrophages were predominantly found in vascularized CD31$^+$ regions of the stroma where they likely serve iron-handling functions in heme homeostasis [34–36]. Overall, these iron$^+$ macrophages were found as a subpopulation of the total macrophages detected in the whole cross sections of stained tissues. Characterization of these general populations indicated that frequency of CD68$^+$ macrophage infiltrates remained approximately unchanged with USPIO injection and further confirmed previous studies indicating that phenotypic inflammatory M1-like macrophage markers are increased and protumor M2-like phenotypes decreased with USPIO injection.

In our spatial analysis, we further characterized effects of USPIO on polarized endogenous and nanoparticle-enhanced iron$^+$ macrophage deposits. We observed that USPIO injections increase iron in pan-macrophage CD68$^+$ populations as expected and also found relative differences in frequency of iron-laden populations following USPIO injection in polarized subsets. Here, although inflammatory (AIF1$^+$), wound-healing (CD206$^+$), and double-positive macrophage populations (AIF1$^+$CD206$^+$) all increased frequency with USPIO injection, inflammatory macrophage populations experienced the largest relative increases presumably due to their predominant role in iron scavenging during the acute inflammatory response caused by the iron nanoparticles [22–24]. Therefore, spatial histological segmentation approaches based on iron status combined with macrophage polarization measurements in these regions allow for the further characterization of subpixel phenotypes of the iron-laden macrophage giving rise to the contrast measured by MRI. This provides further insight into the biological function of the macrophages detected and reveals differences in their iron handling roles in the tumor microenvironment.

4. Conclusions

While the spatial image analysis approach described here is based on identification of the macrophage according to the iron status, similar machine-based analyses are envisioned to be conducted utilizing other parametric MRI contrasts and other multimodality imaging contrasts. Further, in the current work, the approach is specific for the macrophage due to their high innate capacity for iron uptake; however, integrating other endogenous and contrast-agent enhanced parameters with these analysis tools can also potentially provide spatial information about different cellular populations in diverse tissues settings. We anticipate that the current findings will motivate the use of computer-assisted image analysis routines and accelerate the translation of these methods towards the clinic to aid in our imaging investigations of complex cellular microenvironments and physiological processes in diseases such as cancer.

5. Methods

5.1. Animal Procedures. All animal work was approved and performed according to the guidelines of the Animal Care and Use Committee of MSKCC. Mice were anesthetized with 1–3% isoflurane in O_2 gas, and respiration was monitored during all imaging sessions. Female 6-week-old FVB/N mice underwent orthotopic injection into the lower mammary fat pad of 1×10^6 syngeneic TS1 MMTV-PyMT tumor cells grown under standard tissue culture conditions and suspended in 100 μL 50% Matrigel (BD Bioscience). Mice bearing orthotopic TS1 MMTV-PyMT tumors (approximately 1 cm^3) were injected with either 0.5 mmol/kg dextran coated superparamagnetic 5 nm iron oxide nanoparticle contrast agent (Ocean NanoTech) or saline and were imaged 24 hr after injection.

5.2. MRI. ^{1}H MRI was conducted on a 7T/30 cm horizontal bore Biospec MRI system (Bruker BioSpin Corporation) with a custom-built 30 mm inner-diameter transmit-receive quadrature coil. A 2D multigradient echo (MGE) relaxometry pulse sequence with fat suppression was used with the following parameters: 16 evenly spaced 3 ms TEs, TR 1.2 s, matrix 256×256 in the plane data matrix with 25–49 slices, an in-plane spatial resolution of 0.1 mm × 0.1 mm with a slice thickness of 0.5 mm, and RF flip angle of 90°. Each phase encode acquisition was gated on the animal's respiratory cycle. The first image of the gradient-echo series was used as reference images shown in the figures.

Aqueous solutions of $Fe^{3+}(NO_3^-)_3$ (Fisher Scientific) were used as reference iron concentrations over the 0.0–0.3 mg iron(III) g^{-1} range at 7T [29]. The T_2^* values for these solutions were determined by pixel-wise monoexponential fitting of the MGE images using Matlab (Mathworks) and/or Fiji [37]. A linear relation between the relaxation rate $R_2^* = 1/T_2^*$ and known iron concentration was found and was subsequently used to generate parametric iron MRI maps. Iron MRI maps were stratified by high concentration (total range, 0.0–0.3 mg·g^{-1}; high, 0.15–0.3 mg·g^{-1}). Spatial characteristics of the high-iron pixels were then quantified by performing cluster analysis over whole tissue MRI cross sections with the Fiji Analyze Cluster tool.

5.3. Histology. Whole tissue cross sections were sliced from the axial midpoint regions of PBS-perfused tumors following MRI studies, fixed in 4% PFA for 24 hours at 4°C, and then washed with H_2O and resuspended in 70% ethanol (Fisher Scientific). Tissues were paraffin embedded, cut into 5 μm sections, and placed on glass slides for immunohistochemistry.

The Prussian blue histochemical detection of iron(III) was performed by manually deparaffinizing in xylene and rehydration in series of alcohol dilutions (100%, 95%, and 70%) and tap water. Slides were then placed in a working solution of equal parts of 10% potassium ferricyanide (Fisher Scientific) and 10% hydrochloric acid (Fisher Scientific) prepared in distilled water and stained for 30 minutes. Slides were rinsed in distilled water, counterstained with nuclear-fast red, and cover slipped with Permount (Fisher Scientific).

The immunofluorescent detection of F4/80, CD31, CD68, AIF1, and CD206 was performed using a Discovery XT processor (Ventana Medical Systems). The tissue sections were deparaffinized with EZPrep buffer (Ventana Medical Systems), antigen retrieval was performed with the CC1 buffer (Ventana Medical Systems), and sections were blocked for 30 minutes with Background Buster solution (Innovex) followed by avidin/biotin blocking for 8 minutes. F4/80 (Abcam, cat# ab6640, 5 μg/ml), CD31 (Dianova, cat# DIA-310 1 μg/ml), CD68 (Boster, cat# PA1518, 5 μg/ml), AIF1(Wako, cat# 019–19741, 0.5 μg/ml), and CD206 (Abcam, cat# ab64693, 1 μg/ml) were applied, and sections were incubated for 5 hours, followed by 60 minutes incubation with biotinylated goat anti-rabbit antibodies (Vector Labs, cat# PK6101) at 1 : 200 dilution. The detection was performed with Streptavidin-HRP D (part of the DABMap kit, Ventana Medical Systems), followed by incubation with Tyramide Alexa Fluor A488 (Invitrogen, cat# T20922), Tyramide Alexa Fluor 568 (Invitrogen, cat# T20948), or Tyramide Alexa 647 (Invitrogen, cat# B40958), respectively, prepared according to manufacturer's instructions with predetermined dilutions. After staining, slides were counterstained with DAPI (Sigma-Aldrich, cat# D9542, 5 μg/ml) for 10 min and coverslipped with Mowiol. Histological sections were digitized with a Mirax Scan system and read with Panoramic Viewer (3DHISTECH, Budapest, Hungary). Images were first visually inspected, and then the whole images were exported and processed in Fiji. Iron deposits were quantified as described by Leftin et al. [29]. Briefly, iron deposit maps were generated by resizing the histological images by using pixel averaging and bilinear interpolation to down-sample the image size (1 : 100) to the resolution of the MRI experiment. The resulting masks of regions containing iron$^+$ macrophages were discretized by watershed gradient processing, and spatial characteristics of the clusters were determined using the Fiji Analyze Cluster tool. The number of iron$^+$ macrophages per cluster was then determined by using the cluster maps to define regions of interest for cell counts in the full-resolution histological images. Polarization state was determined by either exhaustive whole cross section counting of AIF1 or CD206 immunostained macrophages or localized analysis that was restricted to colocalized iron$^+$ macrophages contained in the iron deposit regions.

5.4. Statistics. Two-tailed Student's t-tests were performed with significance determined as $p < 0.05$. All statistical calculations indicated in the text were performed with the GraphPad Prism 7 Software.

Data Availability

All supporting data are found in the manuscript.

Conflicts of Interest

The authors declare that they have no conflicts of interest.

Acknowledgments

We thank the Molecular Cytology Core Facility at the Memorial Sloan Kettering Cancer Center for histological processing services. This study was funded by National Institutes of Health PO1 (CA115675) and P30 (CA008748), Department of Defense (BC161705), and the National Cancer Institute Kirschstein National Research Service Award Individual Postdoctoral Fellowship (1F32CA206277).

References

[1] R. Weissleder and M. Nahrendorf, "Advancing biomedical imaging," *Proceedings of the National Academy of Sciences*, vol. 112, no. 47, pp. 14424–14428, 2015.

[2] J. R. McCarthy and R. Weissleder, "Multifunctional magnetic nanoparticles for targeted imaging and therapy," *Advanced Drug Delivery Reviews*, vol. 60, no. 11, pp. 1241–1251, 2008.

[3] H. E. Daldrup-Link, "Ten things you might not know about iron oxide nanoparticles," *Radiology*, vol. 284, no. 3, pp. 616–629, 2017.

[4] G. B. Toth, C. G. Varallyay, and A. Horvath, "Current and potential imaging applications of ferumoxytol for magnetic resonance imaging," *Kidney International*, vol. 92, no. 1, pp. 47–66, 2017.

[5] J. Condeelis and R. Weissleder, "*In vivo* imaging in cancer," *Cold Spring Harbor Perspectives in Biology*, vol. 2, no. 12, article a003848, 2010.

[6] M. A. Miller, S. Arlauckas, and R. Weissleder, "Prediction of anti-cancer nanotherapy efficacy by imaging," *Nanotheranostics*, vol. 1, no. 3, pp. 296–312, 2017.

[7] R. Weissleder, M. C. Schwaiger, S. S. Gambhir, H. Hricak et al., "Imaging approaches to optimize molecular therapies," *Science Translational Medicine*, vol. 8, no. 355, article 355ps16, 2016.

[8] W. Liu and J. A. Frank, "Detection and quantification of magnetically labeled cells by cellular MRI," *European Journal of Radiology*, vol. 70, no. 2, pp. 258–264, 2009.

[9] R. Kuhlpeter, H. Dahnke, L. Matuszewski et al., "R_2 and R_2^* mapping for sensing cell-bound superparamagnetic nanoparticles: *in vitro* and murine *in vivo* testing," *Radiology*, vol. 245, no. 2, pp. 449–457, 2007.

[10] J. Zhang, H. L. Ring, K. R. Hurley et al., "Quantification and biodistribution of iron oxide nanoparticles in the primary clearance organs of mice using T1 contrast for heating," *Magnetic Resonance in Medicine*, vol. 78, no. 2, pp. 702–712, 2017.

[11] R. P. Moonen, P. van der Tol, S. J. C. G. Hectors, L. W. E. Starmans, K. Nicolay, and G. J. Strijkers, "Spin-lock MR enhances the detection sensitivity of superparamagnetic iron oxide particles," *Magnetic Resonance in Medicine*, vol. 74, no. 6, pp. 1740–1749, 2015.

[12] S. Liu, S. Buch, Y. Chen et al., "Susceptibility-weighted imaging: current status and future directions," *NMR Biomed*, vol. 30, no. 4, p. e3552, 2017.

[13] R. Fischer and P. R. Harmatz, "Non-invasive assessment of tissue iron overload," *Hematology*, vol. 2009, no. 1, pp. 215–221, 2009.

[14] M. W. Garbowski, J.-P. Carpenter, G. Smith et al., "Biopsy-based calibration of $T2^*$ magnetic resonance for estimation of liver iron concentration and comparison with R2 Ferriscan," *Journal of Cardiovascular Magnetic Resonance*, vol. 16, no. 1, pp. 1–40, 2014.

[15] A. Neuwelt, N. Sidhu, C.-A. A. Hu, G. Mlady, S. C. Eberhardt, and L. O. Sillerud, "Iron-based superparamagnetic nanoparticle contrast agents for MRI of infection and inflammation," *American Journal of Roentgenology*, vol. 204, no. 3, pp. w302–w313, 2014.

[16] E. M. Shapiro, S. Skrtic, K. Sharer, J. M. Hill, C. E. Dunbar, and A. P. Koretsky, "MRI detection of single particles for cellular imaging," *Proceedings of the National Academy of Sciences*, vol. 101, no. 30, pp. 10901–10906, 2004.

[17] S. Jaiswal, M. P. Chao, R. Majeti, I. L. Weissman et al., "Macrophages as mediators of tumor immunosurveillance," *Trends in Immunology*, vol. 31, no. 6, pp. 212–219, 2010.

[18] R. Noy and J. W. Pollard, "Tumor-associated macrophages: from mechanisms to therapy," *Immunity*, vol. 17, pp. 49–61, 2014.

[19] B. Ruffell and L. M. Coussens, "Macrophages and therapeutic resistance in cancer," *Cancer Cell*, vol. 27, no. 4, pp. 462–472, 2015.

[20] G. Corna, L. Campana, E. Pignatti et al., "Polarization dictates iron handling by inflammatory and alternatively activated macrophages," *Haematologica*, vol. 95, no. 11, pp. 1814–1822, 2010.

[21] S. Recalcati, M. Locati, E. Gammella, P. Invernizzi, G. Cairo et al., "Iron levels in polarized macrophages: regulation of immunity and autoimmunity," *Autoimmunity Reviews*, vol. 11, no. 12, pp. 883–889, 2012.

[22] M. Costa da Silva, M. O. Breckwoldt, F. Vinchi et al., "Iron induces anti-tumor activity in tumor-associated macrophages," *Frontiers in Immunology*, vol. 8, p. 1479, 2017.

[23] A. Laskar, J. Eilertsen, W. Li, X.-M. Yuan et al., "SPION primes THP1 derived M2 macrophages towards M1-like macrophages," *Biochemical and Biophysical Research Communications*, vol. 441, no. 4, pp. 737–742, 2013.

[24] S. Zanganeh, G. Hutter, R. Spitler et al., "Iron oxide nanoparticles inhibit tumour growth by inducing pro-inflammatory macrophage polarization in tumour tissues," *Nature Nanotechnology*, vol. 11, no. 11, pp. 986–994, 2016.

[25] A. J. Tavares, W. Poon, Y.-N. Zhang et al., "Effect of removing Kupffer cells on nanoparticle tumor delivery," *Proceedings of the National Academy of Sciences*, vol. 114, no. 51, pp. E10871–E10880, 2017.

[26] R. A. Brooks, J. Vymazal, C. D. Baumgarner, V. Tran, J. W. M. Bulte et al., "Comparison of T2 relaxation in blood, brain, and ferritin," *Journal of Magnetic Resonance Imaging*, vol. 5, no. 4, pp. 446–450, 1995.

[27] K. R. Thulborn, A. G. Sorensen, N. W. Kowall et al., "The role of ferritin and hemosiderin in the MR appearance of cerebral hemorrhage: a histopathologic biochemical study in rats," *American Journal of Roentgenology*, vol. 154, no. 5, pp. 1053–1059, 1990.

[28] X. Zhou, R. L. Magin, J. C. Alameda, H. A. Reynolds, and P. C. Lauterbur, "Three-dimensional NMR microscopy of rat spleen and liver," *Magnetic Resonance in Medicine*, vol. 30, no. 1, pp. 92–97, 1993.

[29] A. Leftin, N. Ben-Chetrit, F. Klemm, J. A. Joyce, and J. A. Koutcher, "Iron imaging reveals tumor and metastasis macrophage hemosiderin deposits in breast cancer," *PLoS One*, vol. 12, no. 9, Article ID e0184765, 2017.

[30] A. Leftin, H. Zhao, M. Turkekul, E. de Stanchina, K. Manova, and J. A. Koutcher, "Iron deposition is associated with differential macrophage infiltration and therapeutic response to iron chelation in prostate cancer," *Scientific Reports*, vol. 7, no. 1, p. 11632, 2017.

[31] S. Gordon, A. Pluddemann, and F. M. Estrada, "Macrophage heterogeneity in tissues: phenotypic diversity and functions," *Immunological Reviews*, vol. 262, no. 1, pp. 36–55, 2014.

[32] E. Van Overmeire, D. Laoui, J. Keirsse, J. A. Van Ginderachter, and A. Sarukhan, "Mechanisms driving macrophage diversity and specialization in distinct tumor microenvironments and parallelisms with other tissues," *Frontiers in Immunology*, vol. 5, p. 127, 2014.

[33] A. Sica and A. Mantovani, "Macrophage plasticity and polarization: *in vivo* veritas," *Journal of Clinical Investigation*, vol. 122, no. 3, pp. 787–795, 2012.

[34] C. E. Lewis and J. W. Pollard, "Distinct role of macrophages in different tumor microenvironments," *Cancer Research*, vol. 15, pp. 605–612, 2006.

[35] J. W. Pollard, "Tumor-educated macrophages promote tumor progression and metastasis," *Nature Reviews Cancer*, vol. 4, no. 1, pp. 71–78, 2004.

[36] E. Gammella, P. Buratti, G. Cairo, and S. Recalcati, "Macrophages: central regulators of iron balance," *Metallomics*, vol. 6, no. 8, pp. 1336–1345, 2014.

[37] J. Schindelin, I. Arganda-Carreras, E. Frise et al., "Fiji: an open-source platform for biological-image analysis," *Nature Methods*, vol. 28, no. 7, pp. 676–682, 2012.

Author(s) Name(s)

It is very important to confirm the author(s) last and first names in order to be displayed correctly on our website as well as in the indexing databases:

Author 1
Given Names: Avigdor
Last Name: Leftin

Author 2
Given Names: Jason A.
Last Name: Koutcher

It is also very important for each author to provide an ORCID (Open Researcher and Contributor ID). ORCID aims to solve the name ambiguity problem in scholarly communications by creating a registry of persistent unique identifiers for individual researchers.

To register an ORCID, please go to the Account Update page (http://mts.hindawi.com/update/) in our Manuscript Tracking System and after you have logged in click on the ORCID link at the top of the page. This link will take you to the ORCID website where you will be able to create an account for yourself. Once you have done so, your new ORCID will be saved in our Manuscript Tracking System automatically.